arTs Università degli Studi di Trieste
Archivio della ricerca – postprint

The mitochondrial protein Opa1 promotes adipocyte browning that is dependent on urea cycle metabolites

Camilla Bean[1,2], Matteo Audano[3], Tatiana Varanita[1,2], Francesca Favaretto[4], Marta Medaglia[1,2], Marco Gerdol[5], Lena Pernas[1,2], Fabio Stasi[4], Marta Giacomello[1], Stèphanie Herkenne[1,2], Maheswany Muniandy[6], Sini Heinonen[6], Emma Cazaly[7], Miina Ollikainen[7], Gabriella Milan[4], Alberto Pallavicini[5], Kirsi H. Pietiläinen[6,8], Roberto Vettor[4], Nico Mitro[3] and Luca Scorrano[1,2] ✉

White to brown/beige adipocytes conversion is a possible therapeutic strategy to tackle the current obesity epidemics. While mitochondria are key for energy dissipation in brown fat, it is unknown if they can drive adipocyte browning. Here, we show that the mitochondrial cristae biogenesis protein optic atrophy 1 (Opa1) facilitates cell-autonomous adipocyte browning. In two cohorts of patients with obesity, including weight discordant monozygotic twin pairs, adipose tissue *OPA1* levels are reduced. In the mouse, *Opa1* overexpression favours white adipose tissue expandability as well as browning, ultimately improving glucose tolerance and insulin sensitivity. Transcriptomics and metabolomics analyses identify the Jumanji family chromatin remodelling protein Kdm3a and urea cycle metabolites, including fumarate, as effectors of *Opa1*-dependent browning. Mechanistically, the higher cyclic adenosine monophosphate (cAMP) levels in *Opa1* pre-adipocytes activate cAMP-responsive element binding protein (CREB), which transcribes urea cycle enzymes. Flux analyses in pre-adipocytes indicate that Opa1-dependent fumarate accumulation depends on the urea cycle. Conversely, adipocyte-specific *Opa1* deletion curtails urea cycle and beige differentiation of pre-adipocytes, and is rescued by fumarate supplementation. Thus, the urea cycle links the mitochondrial dynamics protein Opa1 to white adipocyte browning.

Adipose tissue dysfunction is associated with the fastest growing epidemy in the world, including obesity and obesity-related diseases such as type 2 diabetes mellitus (T2DM), cardiovascular diseases (CVDs) and certain cancers[1]. Altered adipose tissue capacity to store triglycerides (TGs) can lead to insulin resistance and related metabolic complications in individuals with abnormally increased (obesity) or reduced (lipoatrophy) body fat[2]. Because adipose tissue is also an endocrine organ secreting key hormones such as leptin and adiponectin, its dysfunction also impacts distant cells and tissues[3].

In mammals, white adipose tissue (WAT) stores energy, whereas brown adipose tissue (BAT) dissipates energy into heat through uncoupling protein 1 (UCP1)-mediated thermogenesis[4]. In adults, brown fat can counteract obesity and diabetes[5]. Brown-like, beige or brite adipocytes identified in WAT[6,7] can acquire thermogenic properties and become UCP1-positive following exposure to certain adrenergic stimuli, cold or exercise[8,9]. As in humans BAT is scarce, the 'brown conversion' of white fat represents a promising strategy to counteract obesity and metabolic dysfunctions.

Mitochondria are central organelles in adipocyte biology. In BAT, they drive non-shivering thermogenesis, which depends on proton leak across their inner membrane[5]. Not surprisingly, defects in electron transport chain (ETC) activity or fatty acid oxidation (FAO) are hence linked with obesity and metabolic diseases[10,11]. The cellular control over the core energy conversion system of mitochondria can be achieved by the dynamic modulation of mitochondrial shape and morphology, to fine tune respiratory efficiency and nutrient utilization[12,13]. It is therefore not surprising that aberrant mitochondrial morphology is associated with the development of obesity-associated metabolic complications. In muscle, levels of mitochondrial fusion or fission proteins associate with insulin resistance and obesity and mitochondria of diabetes patients are smaller and their cristae are disrupted[14,15]. At the central level, proopiomelanocortin (POMC) neurons require changes in mitochondrial morphology and proximity to the endoplasmic reticulum to govern nutrients sensing and response[16]. The role of the core mitochondrial fusion proteins Opa1 and mitofusin (Mfn) 1 and 2 or of the core fission proteins dynamin-related protein 1 (Drp1) and its adaptors in the adipose tissue is conversely less clear[17]. Deletion of Mfn2 in adipose tissue impairs thermogenesis, yet it protects from high-fat diet[18,19]. A similar resistance to obesity was recorded in a mouse model of Opa1 haploinsufficiency[20], and Opa1 knockout in BAT stimulates WAT browning by inducing expression and secretion of fibroblast growth factor 21 (FGF21)[21]. While a model integrating these results would predict that higher adipose tissue mitochondrial fusion predisposes to obesity, the picture is more complex, because adipose tissue mitochondria appear morphologically and functionally heterogenous. For example, in BAT a peri-droplet

[1]Department of Biology, University of Padova, Padova, Italy. [2]Veneto Institute of Molecular Medicine, Padova, Italy. [3]Department of Pharmacological and Biomolecular Sciences, University of Milan, Milan, Italy. [4]Department of Medicine, University of Padova, Padova, Italy. [5]Department of Life Science, University of Trieste, Trieste, Italy. [6]Obesity Research Unit, Research Program for Clinical and Molecular Metabolism, Faculty of Medicine, University of Helsinki, Helsinki, Finland. [7]Institute for Molecular Medicine Finland, Helsinki Institute of Life Science, University of Helsinki, Helsinki, Finland. [8]Obesity Centre, Abdominal Centre, Helsinki University Hospital and University of Helsinki, Helsinki, Finland. ✉e-mail: luca.scorrano@unipd.it

mitochondrial population provides citrate for lipogenesis whereas a peripheral population performs FAO[22]. It is therefore unclear whether more adipose tissue mitochondrial fusion corresponds to a worse prognosis for obesity. Even less clear is the role of mitochondria in white to brown adipocyte conversion.

We set out to investigate the role of mitochondria-shaping proteins in adipose tissue. In cohorts of patients with obesity, we found a correlation between adipose tissue *OPA1* reduction and increased body weight, even before the onset of clinical complications. By integrating mouse genetics with unbiased approaches, we demonstrate that adipocyte Opa1 regulates adipose tissue expandability and promotes WAT to BAT remodelling via an unexpected axis involving urea cycle stimulation, fumarate accumulation and the Jumanji family histone demethylase Kdm3a.

Results

Decreased adipose tissue *OPA1* expression in human obesity. Because obesity is a complex phenotype caused by the interaction of multiple genetic and environmental factors, twin studies can provide insights into acquired obesity[23]. Thus, we examined whether differences in expression levels of key regulators of mitochondrial morphology are found between monozygotic co-twins discordant for body mass index (BMI) (within-pair difference of BMI $\geq 3\,kg\,m^{-2}$). Gene expression analyses (corrected for age, sex and smoking using the Limma package in Bioconductor) revealed that *OPA1* was significantly downregulated in the subcutaneous adipose tissue (SAT) of heavier co-twins (Fig. 1a), whereas we did not detect any significant difference in *MFN1* and *MFN2* level (Fig. 1b, c). Among the fission genes, only *DRP1* expression was significantly higher in the heavier individuals of the BMI-discordant twin pairs (Fig. 1d, e). Because the mitochondrial transcriptional signature is downregulated in obese monozygotic twins[24], we verified whether *OPA1* and *DRP1* levels correlated with expression of mitochondrial genes. Only *OPA1* significantly correlated with increased mitochondrial gene expression (higher in lean individuals), whereas the correlation between *DRP1* levels and mitochondrial gene expression was not conclusive (Fig. 1f, g). When we connected for both individuals and within pairs a panel of adiposity and insulin resistance measurements with the levels of these mitochondria-shaping genes in a regression model corrected for age, sex and smoking, only *OPA1* expression negatively associated with intra-abdominal fat volume and insulin resistance, both key predictors of metabolic dysfunction (Fig. 1h)[25]. Finally, *OPA1* levels were similarly reduced in visceral adipose tissue (VAT) from stage III–IV patients with obesity or with obesity and diabetes (Supplementary Table 1), while levels of the other mitochondria-shaping genes were similar between normal weight individuals and patients with obesity or with obesity and diabetes (Fig. 1i–m). Taken together, these data suggest a link between lower adipose tissue levels of *OPA1* and obesity and its comorbidities in humans.

Improved adipose tissue function in *Opa1^{tg}* mice. To understand how increased adipose tissue *OPA1* levels were associated with lower BMI and better prognostic indices of metabolic disease in humans we analysed adipose tissue and metabolic function of a mouse model of ubiquitous mild *Opa1* overexpression generated in our laboratory by targeted transgenesis (*Opa1^{tg}*)[12,26]. Notably, SAT and VAT depots of 9-month-old *Opa1^{tg}* mice were significantly reduced in size and weight (Fig. 2a,b). Moreover, the size of *Opa1^{tg}* adipocytes was smaller than that of control mice (Fig. 2c,d). The hormone leptin is secreted from adipocytes in proportion to fat mass to control normal energy homeostasis[27]. The reduction of fat stores in *Opa1^{tg}* mice correlated with decreased leptin transcript levels in VAT and reduced leptin circulating levels (Fig. 2e,f). Accordingly, these morphological and functional *Opa1^{tg}* adipose tissue changes correlated with improved glucose tolerance and insulin sensitivity (Fig. 2g,h). *Opa1^{tg}* mice were slightly resistant to high-fat diet (HFD)-induced obesity compared to their littermate controls (Fig. 2i). The lower weight gain of HFD-fed *Opa1^{tg}* mice was not due to decreased food intake (Fig. 2j) and was accompanied by reduced hepatomegaly after 9 weeks of HFD (Fig. 2k). Livers of HFD-fed wild-type (WT) mice displayed the characteristic steatotic pale colour that was less apparent in *Opa1^{tg}* livers (Fig. 2l). Reduced adiponectin and increased leptin levels, a prototypical secretory pattern of dysfunctional adipose tissue, may result in fat accumulation in the liver[28]. Conversely, after HFD-induced weight gain, levels of leptin were reduced and of adiponectin were elevated in *Opa1^{tg}* mice compared to their littermate controls (Fig. 2m,n). Finally, glucose tolerance and insulin sensitivity were improved in HFD-fed *Opa1^{tg}* mice compared to their littermate controls (Fig. 2o,p). These data suggest that Opa1 may enhance adipose tissue expandability thereby reducing the lipotoxic insult in other organs.

Opa1 increases brown fat thermogenic activity. Because thermogenic activity can increase to dissipate excess energy in response to HFD[29], we asked whether the improved metabolic profile of HFD-fed *Opa1^{tg}* mice could also be caused by increased diet-induced thermogenesis. We first analysed histology of HFD-fed *Opa1^{tg}* BAT and found that their adipocytes were smaller to those in WT littermates, with abundant multi-locular lipid droplets (Extended Data Fig. 1a). Transcriptional changes were also evident in BAT isolated from HFD-fed *Opa1^{tg}* mice compared to WT: adipogenic (*Pparγ*, *Pgc1β*) and thermogenic (CideA, Ucp1) genes were significantly increased, whereas the mitochondrial biogenesis gene *Pgc1α* was not (Extended

Fig. 1 | *OPA1* expression is reduced in patients with obesity. a–e, Expression of the mitochondrial fusion *OPA1* (**a**), *MFN1* (**b**), *MFN2* (**c**) genes and the mitochondrial fission genes *DRP1* (**d**) and *FIS1* (**e**) in SAT of lean and heavy BMI-discordant monozygotic co-twins (BMI difference $>3\,kg\,m^{-2}$; $n=26$ pairs). *Y* axis: arbitrary units (a.u.), from the Affymetrix array. NS, not significant. *P* values from two-tailed moderated paired *t*-test, with adjustments for sex, age and twinship: *OPA1*: $P=0.006$, FDR $P=0.026$; *DRP1*: $P=0.011$, FDR $P=0.026$. **f,g**, Correlations between mitochondrial gene expression data and *OPA1* (**f**) and *DRP1* (**g**) gene expression. Significant correlated transcripts (nominal $P<0.05$) are represented by red dots. Data are from Pearson two-tailed correlation analysis. **h**, Associations in twin individuals (Indiv) and twin pairs (Pairs) between the expression of the indicated genes and the indicated clinical traits assessed using linear-mixed and linear models (two-tailed regression analysis). Data are plotted as standardized β regression coefficients with nominal *P* values. ADIPOQ expr, adiponectin gene expression level; IRS2 expr, insulin receptor substrate 2 gene expression level; HOMA-IR, homeostasis model assessment insulin resistance; IA fat vol, intra-abdominal fat volume. $^{*}P<0.05$; $^{**}P<0.01$; $^{***}P<0.001$. OPA1 associations in individuals: IRS ($P=1.3\times10^{-5}$, confidence interval (CI): 0.21–0.26), HOMA ($P=3.6\times10^{-5}$, CI: −0.57 to −0.20), IA fat vol ($P=0.001$, CI: −0.66 to −0.16]). OPA1 associations in pairs: IRS ($P=0.004$, CI: 0.11–0.61), HOMA ($P=0.003$, CI:0.58–0.10), IAFAT ($P=0.009$, CI: 0.66 to −0.08); MFN1 associations in individuals: IRS ($P=0.04$, CI: 0.02–0.47), MFN1 associations in pairs: IA fat vol ($P=0.001$, CI: 0.24–1.11). DRP1 associations in individuals: IRS ($P=0.02$, CI: 0.57 to −0.04), HOMA ($P=0.04$, CI: 0.02–0.56), IA fat vol ($P=0.01$, CI: 0.11–0.70), ADIPOQ ($P=0.001$, CI: 0.99 to −1.00). **i–m**, qPCR analysis of the mitochondrial fusion *OPA1* (**i**), *MFN1* (**j**), *MFN2* (**k**) and fission *DRP1* (**l**) and *FIS1* (**m**) transcripts from abdominal wall fat pad biopsies of six lean subjects, 18 normoglycaemic subjects with obesity (obese), and 19 diabetic patients with obesity (obese-T2DM). Data are normalized for the expression of S18. Dots represent individuals; boxes, mean ± s.e.m.; whiskers, 10th and 90th percentiles. $^{*}P=0.012$ Obese versus Lean; $P=0.028$ obese-T2DM versus lean in a Mann–Whitney *U*-test versus lean.

Data Fig. 1b). Even SAT from HFD-fed *Opa1*^{tg} mice displayed certain BAT features compared to WT (that is, *Ucp1*, *Pparγ*, *Pgc1β* induction; Extended Data Fig. 1c), suggesting that Opa1 could play a role in thermogenesis. We therefore decided to analyse BAT function in *Opa1*^{tg} mice. The interscapular brown adipose tissue (iBAT) was classically brown-red in control mice, whereas iBAT was more intensely reddish-brown in *Opa1*^{tg} mice (Fig. 3a). Histological analysis indicated that *Opa1*^{tg} iBAT adipocytes were smaller with more multi-locular lipid droplets (Fig. 3b). Immunostaining (Fig. 3c,d) and quantitative polymerase chain reaction (qPCR; Fig. 3e) confirmed increased *Ucp1* levels in *Opa1*^{tg} iBAT compared to WT. In addition, *Opa1*^{tg} mice were more tolerant to acute cold exposure (Fig. 3f,g). A direct calorimetric experiment in confined metabolic cages proved that *Opa1*^{tg} mice produced more heat at room temperature (RT) as well as when exposed to lower temperatures (Fig. 3h). Analysis of covariance (ANCOVA) test to exclude the confounding

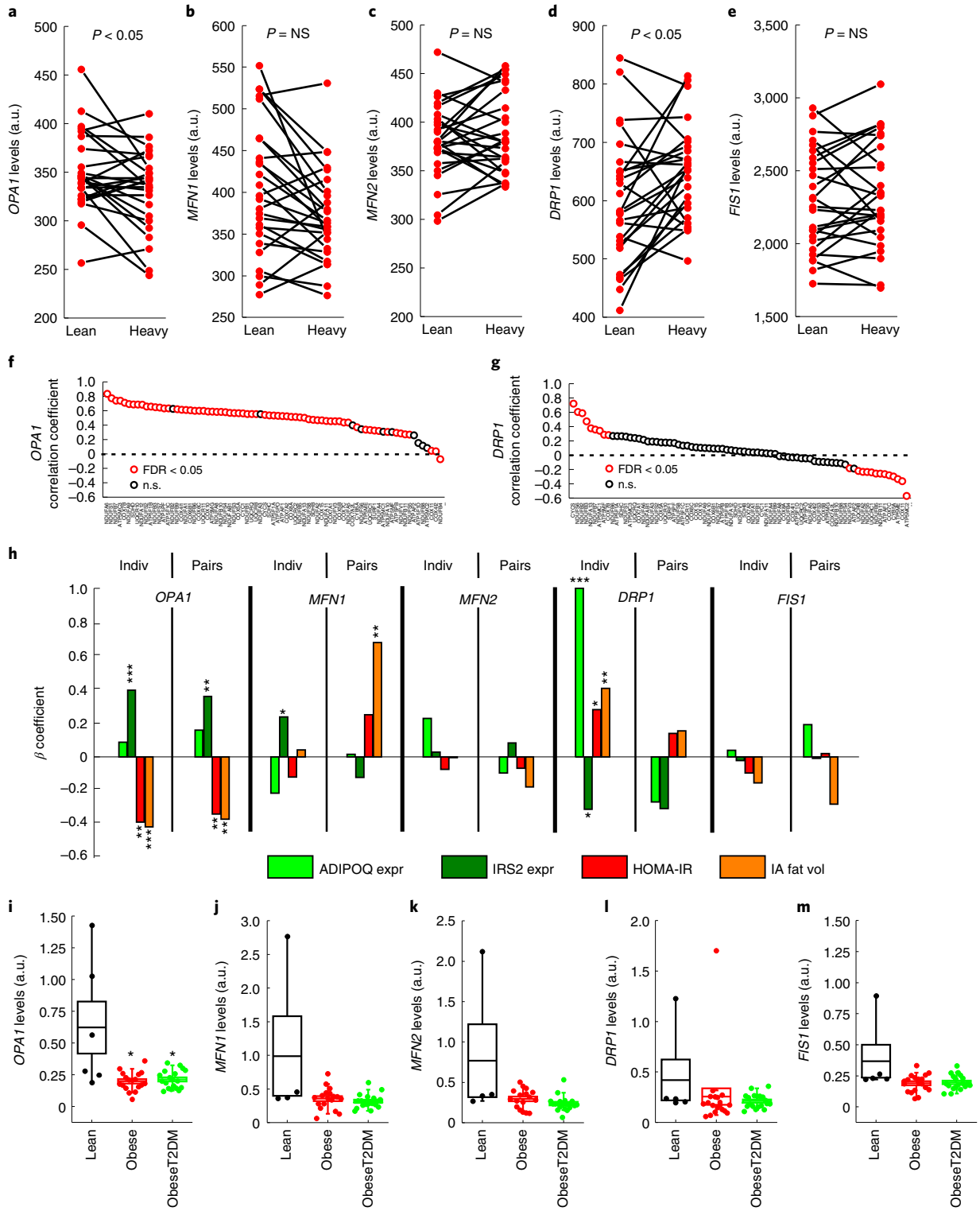

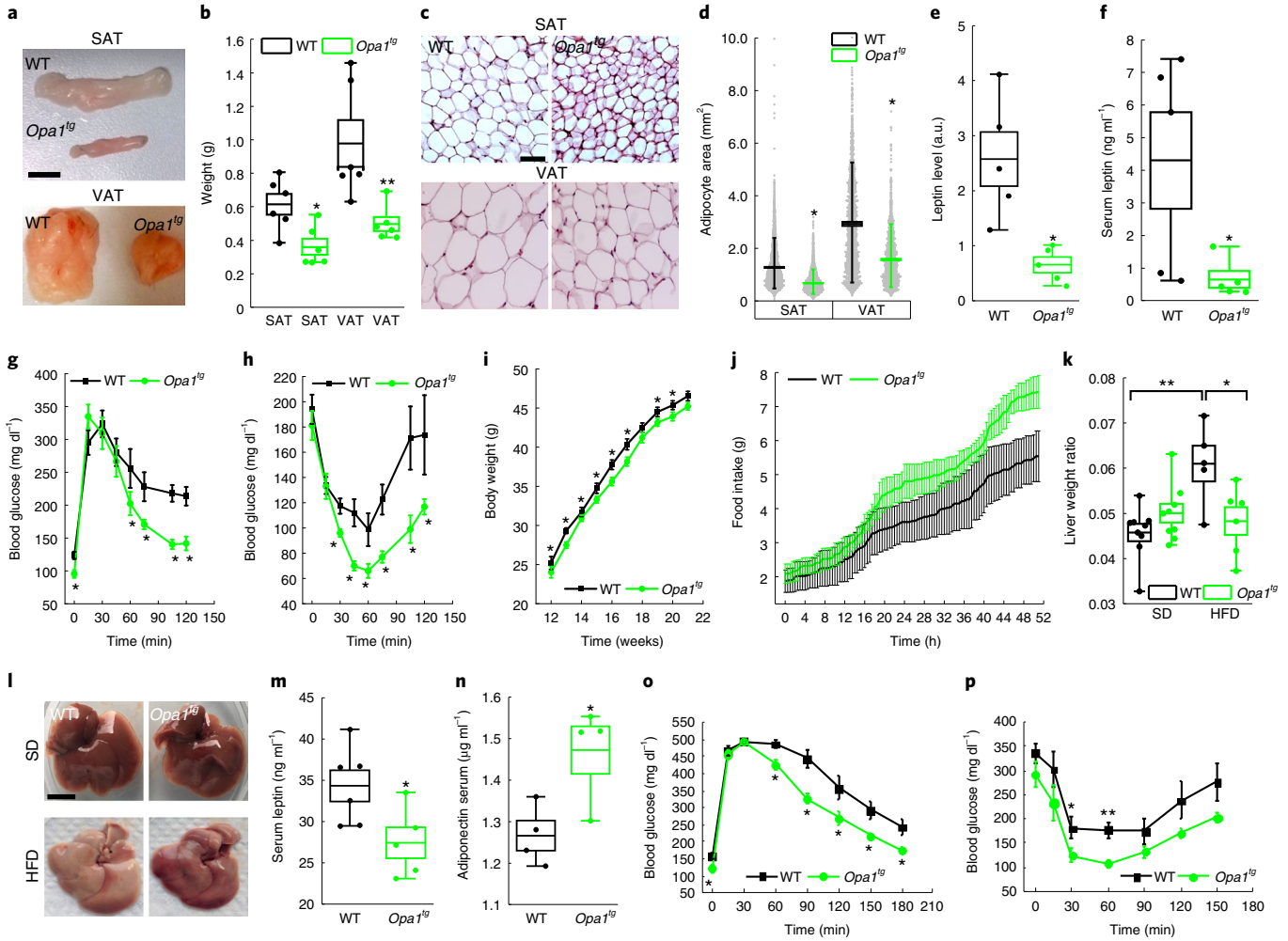

Fig. 2 | *Opa1*^{tg} mice are metabolically healthier on a HFD. a, Representative SAT and VAT photographs in WT and *Opa1*^{tg} mice ($n=6$ per genotype). Scale bar, 1 cm. **b**, SAT and VAT weight in WT and *Opa1*^{tg} mice ($n=6$). $^{*}P=0.020$; $^{**}P=0.008$ in a two-tailed Mann–Whitney *U*-test between *Opa1*^{tg} and WT. **c**, Representative H&E-stained SAT and VAT sections from WT and *Opa1*^{tg} mice ($n=6$ per genotype). **d**, Adipocyte area in WT and *Opa1*^{tg} mice ($n=3{,}200$ adipocytes in WT and 3,474 in *Opa1*^{tg} SAT; 1,677 in WT and 1,543 in *Opa1*^{tg} VAT, four mice per genotype). $^{*}P=0$ in a two-tailed Mann–Whitney *U*-test between WT and *Opa1*^{tg}. **e**, VAT leptin messenger RNA levels in WT and *Opa1*^{tg} mice ($n=5$). $^{*}P=0.012$ in a two-tailed Mann–Whitney *U*-test between *Opa1*^{tg} and WT. **f**, Serum leptin levels in WT and *Opa1*^{tg} mice ($n=5$). $^{*}P=0.036$ in a two-tailed Mann–Whitney *U*-test between *Opa1*^{tg} and WT. **g**,**h**, Average ± s.e.m. blood glucose levels following an intraperitoneal (i.p.) glucose tolerance test (GTT, **g**) or an i.p. insulin tolerance test (ITT, **h**) performed on WT and *Opa1*^{tg} mice ($n=4$ (**g**); $n=4$–6 (**h**)). $^{*}P<0.05$ in a two-tailed Mann–Whitney *U*-test. **i**, Average ± s.e.m. body weight of WT and *Opa1*^{tg} mice fed with a 60% HFD for 9 weeks ($n=8$–9). $^{*}P<0.05$ in a two-tailed Mann–Whitney *U*-test. **j**, Cumulative food intake of HFD-fed WT and *Opa1*^{tg} mice ($n=3$). **k**, Liver/total body weight ratio of WT and *Opa1*^{tg} mice fed with standard diet (SD, $n=9$) or HFD ($n=5$). $^{*}P=0.049$ (HFD versus SD-fed WT); $^{**}P=0.016$ (HFD-fed *Opa1*^{tg} versus WT) in a two-tailed Mann–Whitney *U*-test. **l**, Representative photographs of livers from SD ($n=9$) and HFD ($n=5$) fed WT and *Opa1*^{tg} mice. Scale bar, 1 cm. **m**,**n**, Serum Leptin (**m**) and Adiponectin (**n**) levels in HFD-fed WT and *Opa1*^{tg} mice ($n=4$–6). $^{*}P=0.028$ for leptin and $P=0.0043$ for adiponectin (*Opa1*^{tg} versus WT) in a one-sided Kruskal–Wallis ANOVA. **o**,**p**, Average ± s.e.m. of blood glucose levels following a GTT (**o**) or an ITT (**p**) in HFD-fed WT and *Opa1*^{tg} mice ($n=6$–7). $^{*}P<0.05$; $^{**}P<0.01$ in a two-tailed Mann–Whitney *U*-test. In dot-box plots in panels **b**, **d**, **e**, **f**, **k** and **m**, dots indicate independent measurements; boxes, mean ± s.e.m.; whiskers, 10th and 90th percentiles.

effect of body weight on basal heat production[30] further confirmed the thermogenic effect observed in *Opa1*^{tg} mice (Extended Data Fig. 2a). Heat production was dependent on fat mass, as evident following normalization of calorimetric data for lean and fat mass determined by Echo-magnetic resonance imaging (MRI) measurements in confined metabolic cages at RT and 18 °C (Extended Data Fig. 2b,c). Thus, Opa1 stimulates BAT function.

Opa1 promotes cell-autonomous white pre-adipocytes browning. The improvement in all the metabolic parameters studied in *Opa1*^{tg} mice could be ascribed to the ameliorated BAT function, but also to changes in *Opa1*^{tg} WAT. This latter possibility was suggested by the retrieval of higher *Ucp1* expression in SAT of HFD-fed *Opa1*^{tg} mice compared to their WT littermates (Extended Data Fig. 1c), indicating that Opa1 might promote browning of WAT. In mice, beige adipocytes mainly reside together with unilocular white adipocytes in SAT[31]. We therefore compared levels of Opa1 and other mitochondria-shaping proteins between SAT and VAT. As expected, the brown marker genes *Ucp1*, *CideA* and *Cox8b* were enriched in the browning-prone SAT compared to VAT. *Opa1* was more expressed in SAT, whereas key mitochondrial biogenesis genes and *Mfn1* and *Mfn2* were more expressed in VAT, a depot known to be more mitochondria-rich than SAT (Extended Data Fig. 3a)[32]. Thus, in a major difference from the other mitochondrial fusion genes,

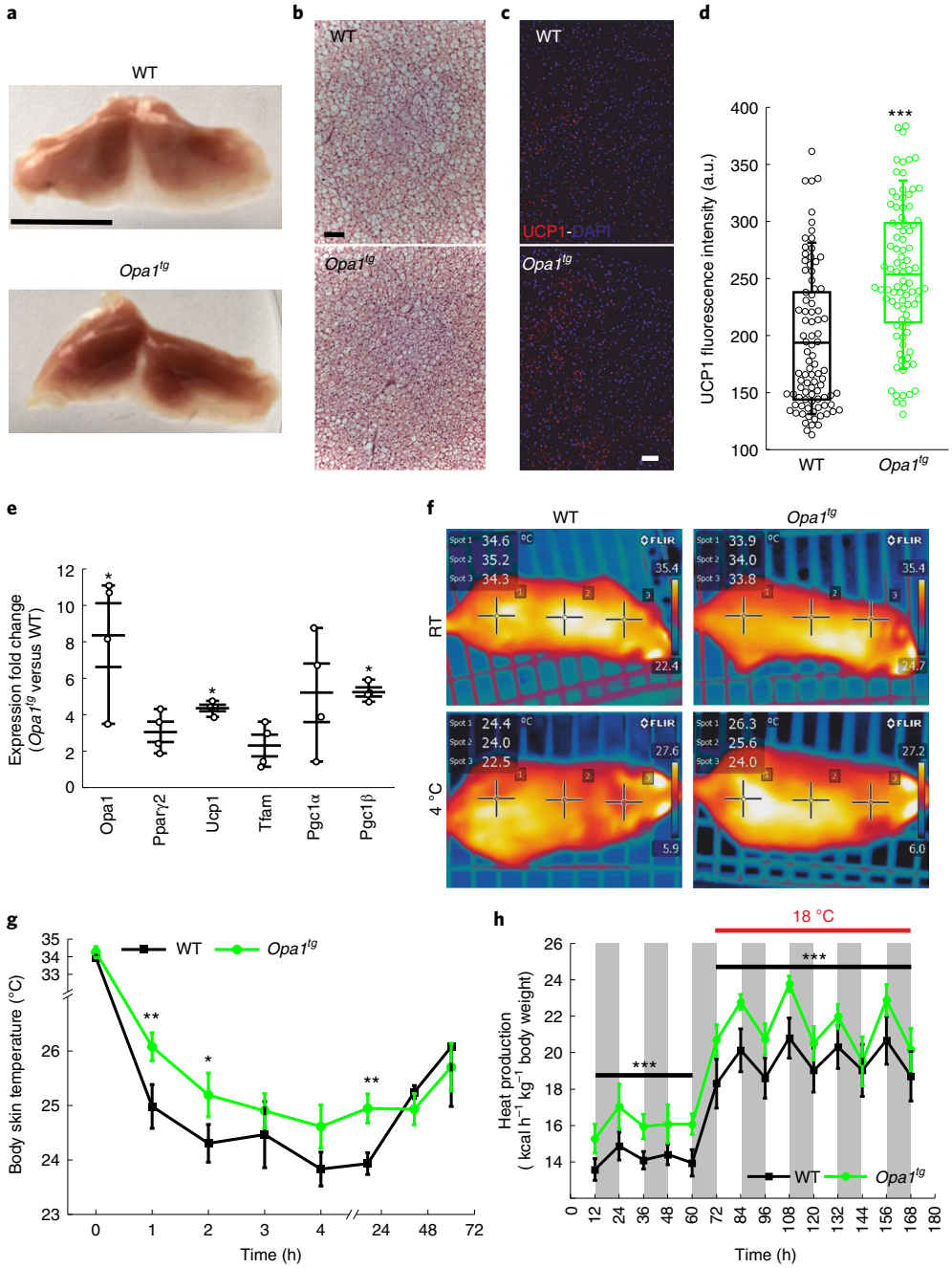

Fig. 3 | Opa1 promotes BAT thermogenic activity. a, Representative photographs of BAT from WT and *Opa1*^{tg} mice ($n = 11$ per genotype). Scale bar, 1 cm. **b**, Representative H&E-stained sections of BAT from WT and *Opa1*^{tg} mice ($n = 4$ per genotype). Scale bar, 50 µm. **c**, Representative fluorescence images of BAT sections from WT and *Opa1*^{tg} mice stained as indicated ($n = 3$ per genotype). Scale bar, 50 µm. **d**, UCP1 staining intensity per tissue area of BAT sections of WT and *Opa1*^{tg} mice ($n = 3$ per genotype). $^{***}P < 0.001$ in a two-tailed Mann–Whitney *U*-test. Dots indicate individual measurements (from $n = 3$ independent experiments); boxes, mean ± s.e.m.; whiskers, 10th and 90th percentiles. **e**, Expression fold change (*Opa1*^{tg} versus WT) of key thermogenic and mitochondrial transcripts in BAT isolated from WT and *Opa1*^{tg} mice ($n = 4$ per genotype). Dots represent independent measurements; lines and whiskers, mean ± s.e.m. $^{*}P = 0.03$ in a two-tailed Mann–Whitney *U*-test. **f**, Representative pseudocoloured dorsal view images of infrared thermography of conscious WT and *Opa1*^{tg} male mice exposed to the indicated temperatures ($n = 4$ per genotype). **g**, Average ± s.e.m. of body skin temperature measured in experiments as in **f** ($n = 4$ per genotype). $^{*}P < 0.05$, $^{**}P < 0.01$ in a two-tailed Mann–Whitney *U*-test. **h**, Average ± s.e.m. of heat release in light and dark (grey vertical stripes) cycles recorded in WT and *Opa1*^{tg} male mice at 24 °C or at the indicated temperature ($n = 7$ per genotype) $^{***}P = 1.95 \times 10^{-4}$ (RT) $P = 4.37 \times 10^{-7}$ (18 °C) *Opa1*^{tg} versus WT in a one-way repeated measures ANOVA.

Opa1 is enriched in the fat depot that can undergo browning in the mouse. More interestingly, thermogenic markers were already higher in *Opa1*^{tg} compared to WT SAT at RT (Fig. 4a). When we exposed mice to 4 °C, UCP1 became detectable in immunoblots of *Opa1*^{tg} SAT (Fig. 4b) and Ucp1 transcript increased 28-fold in *Opa1*^{tg} compared to WT SAT (Fig. 4c). *Opa1*^{tg} mice were also more prone to adrenergic WAT browning. In vivo, β3-adrenergic agonist administration resulted in the formation of BAT-like adipocytes,

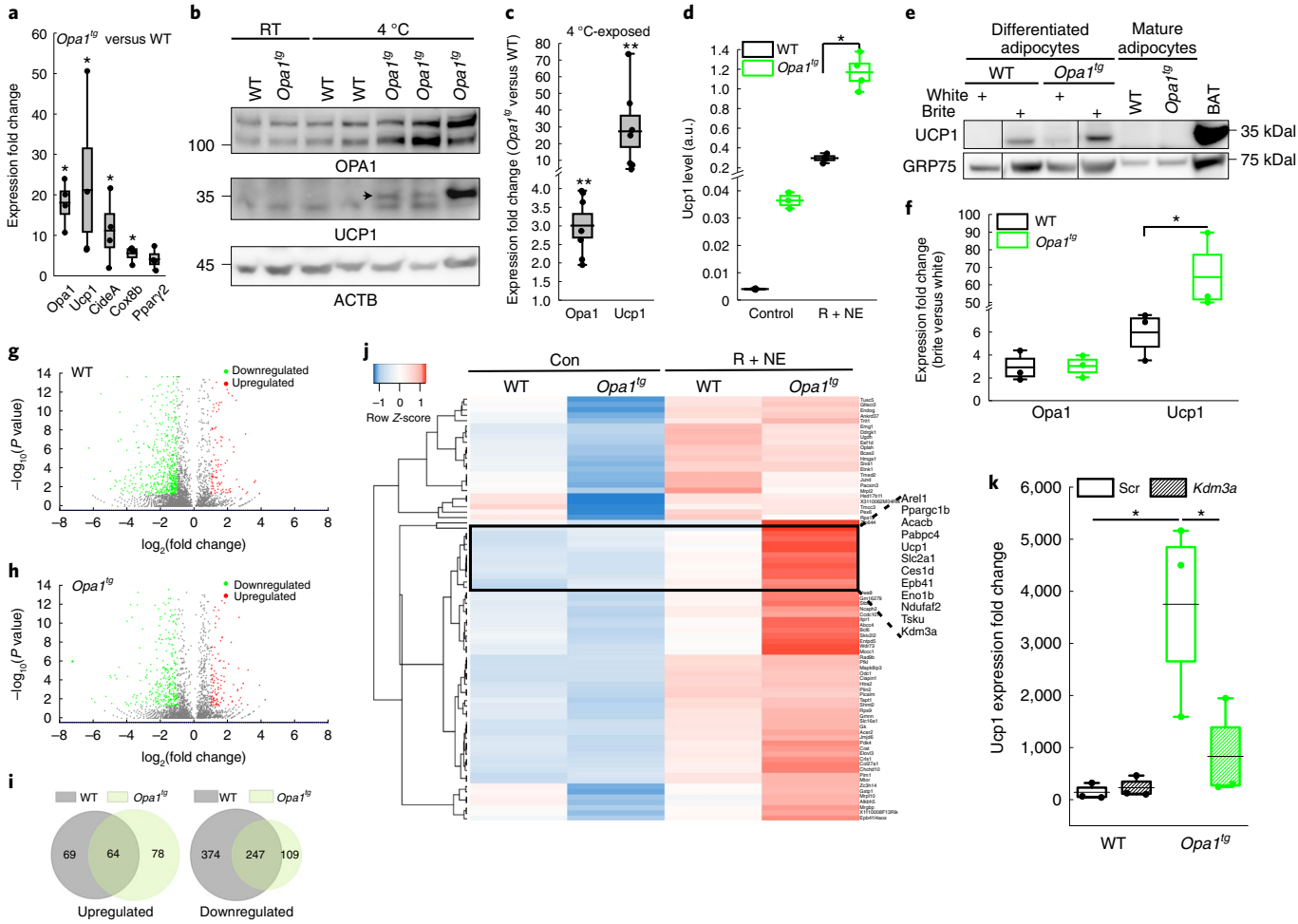

Fig. 4 | Opa1 promotes adipocyte Ucp1 transcription via Kdm3a. a, Expression fold change (*Opa1*^{tg} versus WT) of BAT genes in SAT ($n=4$ per genotype). $^{*}P=0.03$ in a two-tailed Mann–Whitney *U*-test. **b**, Representative immunoblots of equal amounts (20 µg) of SAT lysates from WT and *Opa1*^{tg} littermates housed at RT or cold-exposed (4 °C) for 72 h ($n=3$ independent experiments). Each lane corresponds to an individual mouse. Arrow: UCP1 band. **c**, Expression fold change (*Opa1*^{tg} versus WT) in SAT of cold-exposed mice ($n=7$ per genotype). $^{**}P=0.003$ for Opa1 and $P=0.007$ for Ucp1 in a two-tailed Mann–Whitney *U*-test. **d**, Ucp1 mRNA levels in differentiated WT and *Opa1*^{tg} SAT pre-adipocytes ($n=4$ per genotype). Where indicated, medium contains R + NE to induce browning. $^{*}P=0.03$ in a two-tailed Mann–Whitney *U*-test. **e**, Representative immunoblots of equal amounts (20 µg) of lysates from WT and *Opa1*^{tg} SAT pre-adipocytes differentiated for 7 days into white or brite adipocytes. SAT mature adipocytes of the indicated genotype and WT BAT lysates (20 µg) are loaded as controls ($n=5$ independent experiments). **f**, Expression fold change (brite versus white) in white to brown differentiated samples as in **e**. $^{*}P=0.014$ in a Kruskal–Wallis ANOVA test. **g**,**h**, Volcano plots of DEGs identified in RNA sequencing experiments in pre-adipocytes from pooled ($n=5$) SAT of WT (**g**) or *Opa1*^{tg} (**h**) mice differentiated to brite (R + NE). Coloured dots indicate significant DEGs at $P<0.05$ FDR and twofold change cut-off. **i**, Venn diagrams of DEG sets in **g** and **h**. Numbers of DEGs are indicated. **j**, Heat map of expression levels of an Opa1-specific upregulated gene subset identified in **i**. Each column corresponds to the indicated sample. The dendrogram clusters genes with similar expression profiles. Gene expression levels per row are indicated. **k**, *Ucp1* expression fold change (brite versus pre-adipocytes) in WT and *Opa1*^{tg} SAT pre-adipocytes transduced with the indicated shRNA and differentiated into brite adipocytes ($n=3$ per genotype). $^{*}P=0.049$ in a two-tailed Mann–Whitney *U*-test between the indicated groups. In box-dot plots in panels **a**, **c**, **d**, **f** and **k** dots represent biologically independent experiments; boxes, mean ± s.e.m.; whiskers, 10th and 90th percentiles.

characterized by multi-locular lipid droplets in both *Opa1*^{tg} SAT and VAT (Extended Data Fig. 3b)[32]. Altogether, these data indicate that levels of Opa1 positively correlate with WAT browning capacity. However, they do not clarify whether Opa1 stimulates browning in a cell-autonomous fashion, nor provide hints on the mechanism by which a mitochondrial cristae biogenesis and fusion protein could stimulate the complex process of WAT browning.

To address these two outstanding questions, we turned to primary cultures of pre-adipocytes derived from the vascular stromal fraction of WT and *Opa1*^{tg} SAT, where any pro-browning effect of OPA1 would be cell autonomous, and where we could better investigate molecular mechanisms of browning. We compared the appearance of the brown adipocyte marker UCP1 following 7 days of differentiation in a standard tissue culture medium (con) or in medium supplemented with the peroxisome proliferator-activated receptor γ (PPARγ) agonist rosiglitazone and norepinephrine (R + NE) to favour the emergence of brite cells in white preadipocyte cultures[6]. Absolute levels of *Ucp1* were more robustly increased in primary *Opa1*^{tg} pre-adipocytes cultured in the supplemented medium, suggesting that Opa1 overexpression can cell-autonomously favour WAT browning (Fig. 4d–f). We therefore used this system to gain insight into the molecular mechanism of the pro-browning function of OPA1. Comparison of deep RNA sequencing (RNA-seq) of primary white WT and *Opa1*^{tg} pre-adipocytes performed after 7 days of differentiation in standard culture medium and in the pro-brite medium revealed that 754 and 498 genes were

differentially expressed in brite-differentiated WT and *Opa1*^{tg} adipocytes, respectively (Fig.4g, h; genes are listed in Supplementary Data 1). This unbiased approach substantiates that Opa1 influences gene expression during brite differentiation of WAT pre-adipocytes but does not indicate how Opa1 acts. To answer this question, we started by verifying if an *Opa1*^{tg}-specific signature of differentially expressed genes (DEGs) existed. Venn diagrams indicated that 37% of all upregulated genes were specific for *Opa1*^{tg} preadipocyte differentiation, whereas only 15% of the downregulated genes were *Opa1*^{tg} specific (Fig. 4i). Because we did not find transcription factors or cofactors involved in adipose tissue subtype specification to be downregulated by R+NE treatment of *Opa1*^{tg} pre-adipocytes (Extended Data Fig. 4a), we performed a more detailed analysis of the DEGs specifically upregulated during brite differentiation of *Opa1*^{tg} pre-adipocytes. We verified by average linkage using Pearson's distance measurement which genes among these DEGs clustered with UCP1. We retrieved 11 genes involved in different processes: ubiquitination (*Arel1*)[33], lipid metabolism (*Acacb*[34] and *Ces1d*)[35], transcription (*Pabpc4*)[36], glycolysis (*Eno1b* and *Slc2a1*), cytoskeletal architecture (*Epb41*)[37], mitochondrial biogenesis (*Ppargc1b*[38] and *Ndufaf2*)[39]. Two genes caught our attention: Tsukushi (*Tsku*), a hepatokine implicated in thermogenesis, and *Kdm3a* (also known as Jmjd1A), a member of the Jumanji demethylases, crucial enzymes in epigenetic modulation (Fig. 4j). However, while *Tsku* appears to inhibit thermogenesis and browning[40], an opposite effect to that elicited by Opa1, *Kdm3a* increases brown and beige thermogenic activity by controlling the H3K9 methylation status of *Adrb1* and *Ucp1*[41,42]. We used ingenuity pathway analysis (IPA) to infer if any potential upstream Jumanji family regulators were over-represented during *Opa1*^{tg} preadipocyte brite differentiation. Interestingly, HIF1α, a key regulator of *Kdm3a* expression[43], together with several other hypoxia-related regulators such as CREB[44], MYC[45] and FLI1[46] were predicted to be activated during *Opa1*^{tg} preadipocyte brite differentiation (Extended Data Fig. 4b). Indeed, HIF1α silencing during *Opa1*^{tg} preadipocyte brite differentiation curtailed the increased *Ucp1* expression (Extended Data Fig. 4c). Moreover, IPA revealed the existence of a network ($P=8\times10^{-6}$) where KDM3a and HIF1α were key components in the connection between OPA1 and UCP1 (Extended Data Fig. 4d). We therefore verified whether Opa1 and Kdm3a were in the same pathway of Ucp1 transcription regulation. Efficient retroviral-mediated *Kdm3a* silencing in WT and *Opa1*^{tg} primary white pre-adipocytes (Extended Data Fig. 4e) did not affect Ucp1 induction during brite differentiation of WT cells, whereas it abolished the stimulatory effect measured in *Opa1*^{tg} cells (Fig. 4k). Thus, *Opa1*^{tg} white pre-adipocytes are primed for KDM3a-dependent expression of *Ucp1* in response to a brite differentiation stimulus. The combination of unbiased approaches, bioinformatics and preadipocyte differentiation experiments identify that *Opa1* requires *Kdm3a* to stimulate *Ucp1* expression during adipocyte browning.

Increased urea cycle and fumarate in *Opa1*^{tg} pre-adipocytes. We next wished to understand how Opa1 impinged on Kdm3a. *Kdm3a* is a hypoxia regulated gene and often mitochondrial dysfunction results in a pseudohypoxia response driven by the accumulation of Krebs' cycle intermediates that recruit HIF1α and orchestrate epigenetic changes[47]. However, in *Opa1*^{tg} cells respiration is more efficient and mitochondria are even protected from respiratory chain inhibition[12], reducing the likelihood that tricarboxylic acid (TCA) cycle intermediates accumulate to drive the observed Kdm3a upregulation. Nevertheless, we did not discard a priori this metabolic hypothesis. Indeed, metabolomic profiling indicated that fumarate levels were significantly upregulated in *Opa1*^{tg} SAT pre-adipocytes compared to their WT counterparts. Surprisingly, fumarate appeared as the only TCA metabolite significantly increased in *Opa1*^{tg} SAT pre-adipocytes (Fig. 5a). We therefore tested whether fumarate could link mitochondria and Kdm3a-dependent *Ucp1* expression. We administered dimethyl fumarate (DMF), a cell permeant analogue of fumarate, to WT and *Opa1*^{tg} WAT pre-adipocytes. During adipocyte differentiation of WT pre-adipocytes DMF stimulated a 2.7-fold increase in *Ucp1* expression, whereas the high *Ucp1* expression measured during differentiation of *Opa1*^{tg} WAT pre-adipocytes could not be further boosted by DMF. To address whether *Ucp1* expression induced by DMF was dependent on KDM3a, we efficiently silenced KDM3a in WT and *Opa1*^{tg} pre-adipocytes (WT: 0.26 ± 0.03 in shKdm3a versus shScr; *Opa1*^{tg}: 0.5 ± 0.1 in shKdm3a versus shScr; $n=5$ independent experiments, $P<0.05$ in a non-parametric Kruskal–Wallis test). Silencing of *Kdm3a* in WT pre-adipocytes reduced the *Ucp1* induction by DMF treatment; in *Opa1*^{tg} pre-adipocytes, it curtailed the observed *Ucp1* induction (Fig. 5b). Altogether, these experiments nominate fumarate as a metabolite capable of driving Kdm3a-dependent Ucp1 induction in WAT.

Next, we wished to understand the source of fumarate in *Opa1*^{tg} pre-adipocytes. Fumarate is a TCA intermediate, but other TCA intermediates were not significantly accumulated. We conversely noticed that levels of urea cycle intermediates (arginine, dimethylarginine, ornithine, acetylornithine) and of polyamines that are produced from urea cycle intermediates (spermine, spermidine, putrescine) were significantly increased in *Opa1*^{tg} pre-adipocytes (Fig. 5a). Indeed, a bioinformatic analysis using MetaboAnalyst indicated a clear signature of over-representation of pathways of amino acid disposal and urea cycle in *Opa1*^{tg} pre-adipocytes (Fig. 5c). In steady-state metabolomics of *Opa1*^{tg} SAT we similarly observed an increase in arginine and the polyamine putrescine (Extended Data Fig. 5a). Fumarate was barely detected by metabolomics but in direct measurements it was twofold higher in *Opa1*^{tg} SAT compared to WT (Extended data Fig. 4b). MetaboAnalyst confirmed a similar over-representation of urea cycle also in mature SAT (Extended data Fig. 4c). We therefore verified if urea cycle intermediates and fumarate accumulated specifically during brite differentiation of *Opa1*^{tg} pre-adipocytes. We compared metabolomics data obtained in WT and *Opa1*^{tg} pre-adipocytes and brite adipocytes. Urea cycle intermediates, polyamines and fumarate were over-represented in *Opa1*^{tg} throughout the process of brite differentiation; conversely, citrulline, the key precursor of argininosuccinate that in the urea cycle is converted to arginine and fumarate, was reduced (Fig. 5d)[48]. To verify if indeed the urea cycle was required for Opa1-induced stimulation of preadipocyte browning, we efficiently silenced the urea cycle rate limiting enzyme carbamoyl phosphate synthetase-1 (CPS1) and the enzyme argininosuccinate lyase (ASL) that catalyses the cleavage of argininosuccinate into arginine and fumarate by lentiviral delivery of short hairpin RNAs (shRNAs, Cps1: 0.39 ± 0.03 in WT+shCps1 versus WT+shUT 0.034 ± 0.02 in *Opa1*^{tg}+shCps1 versus *Opa1*^{tg}+shUT, $n=9$–11, $P<0.01$; Asl: 0.48 ± 0.02 in WT+shAsl versus WT+shUT 0.038 ± 0.01 in *Opa1*^{tg}+shAsl versus *Opa1*^{tg}+shUT, $n=12$–15, $P<0.01$). Silencing CPS1 or ASL had no effect on the browning of WT pre-adipocytes, whereas it inhibited browning of white *Opa1*^{tg} pre-adipocytes, bringing it to WT levels (Fig. 5e). Of note, cell permeant fumarate corrected the reduction in browning (measured as Ucp1 expression) caused by Cps1 silencing in *Opa1*^{tg} pre-adipocytes, suggesting a role for urea cycle in the production of fumarate required for Opa1-induced browning (Fig. 5f).

Increased urea cycle flux in *Opa1*^{tg} pre-adipocytes. To understand which metabolic pathway contributed the most to fumarate accumulation in *Opa1*^{tg} pre-adipocytes, we performed two different tracing experiments with [^{13}C3]-pyruvate and [^{13}C4,^{15}N]-L-aspartic acid. [^{13}C3]-pyruvate was used to analyse the contribution of the TCA cycle, while [^{13}C4,^{15}N]-L-aspartic acid was used to test the influence of de novo purine synthesis and urea cycle to fumarate generation. The [^{13}C3]-pyruvate flux analysis indicated that fumarate M2 (fumarate from TCA) increased by 7% in *Opa1*^{tg} compared

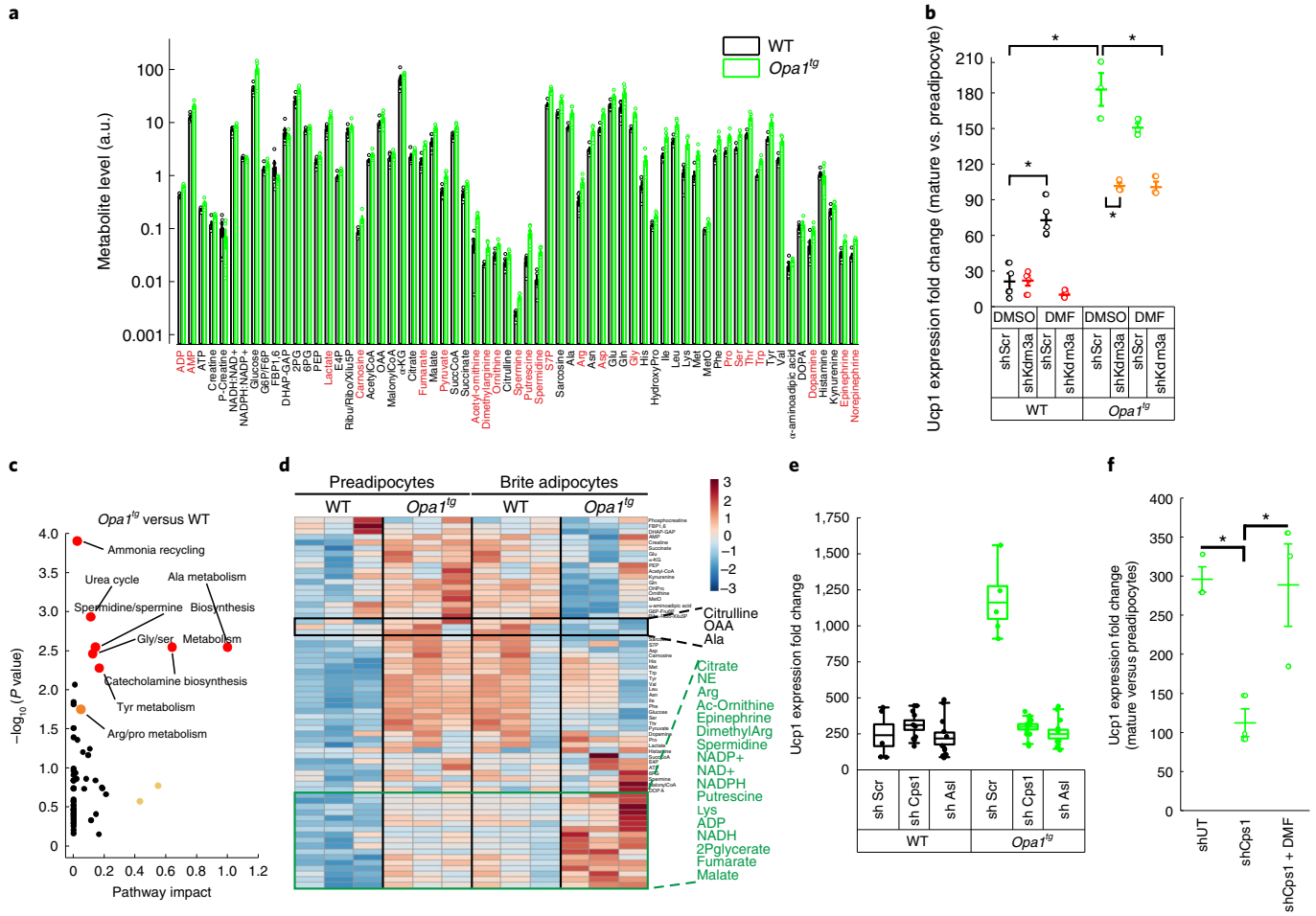

Fig. 5 | Opa1 promotes adipocyte Ucp1 transcription via urea cycle induction. a, Metabolite levels in WT and *Opa1*^{tg} SAT pre-adipocytes. Red named metabolites are significantly different between *Opa1*^{tg} and WT pre-adipocytes at a $P < 0.05$ FDR and 1.75-fold change cut-off in six independent experiments ($n = 3$ mice per genotype). **b**, *Ucp1* expression fold change (brite versus pre-adipocytes) in WT and *Opa1*^{tg} SAT pre-adipocytes transduced with the indicated shRNA and differentiated into brite adipocytes ($n = 3$, $n = 5$). Dots represent biologically independent experiments; lines, mean; whiskers, s.e.m. *$P = 0.01$ for shScr WT versus shScr WT + DMF; $P = 0.03$ for shScr *Opa1*^{tg} versus shScr WT and for shKdm3a *Opa1*^{tg} versus shScr *Opa1*^{tg}; $P = 0.049$ for shKdm3a *Opa1*^{tg} + DMF versus shScr *Opa1*^{tg} in a two-tailed Mann–Whitney *U*-test. **c**, Significant metabolites in **a** were analysed using the pathway analysis module of the MetaboAnalyst tool. Red dots show the top significantly relevant pathways. **d**, Heat map analysis by MetaboAnalyst of metabolites showing the largest change among undifferentiated and brite-differentiated white pre-adipocytes of the indicated genotype. The normalized metabolites levels were converted to z-scores by MataboAnalyst. The heat map scale ranges from -3 to +3 z-score values. **e**, *Ucp1* expression fold change (brite versus pre-adipocytes) in WT and *Opa1*^{tg} pre-adipocytes transduced with the indicated shRNA and differentiated into brite adipocytes ($n = 5$ per condition). Dots represent biologically independent experiments; boxes, mean ± s.e.m.; whiskers, 10th and 90th percentiles. **f**, *Ucp1* expression fold change (mature versus pre-adipocytes) in WT and *Opa1*^{tg} SAT pre-adipocytes transduced with the indicated shRNA, treated where indicated with DMF (40 μM) and differentiated into brite adipocytes ($n = 3$ per condition). Dots represent biologically independent experiments; lines, mean; whiskers, s.e.m. *$P = 0.049$ in a Kruskal–Wallis ANOVA test.

to WT pre-adipocytes (Fig. 6a). Importantly, we observed a marked increase of aspartate M2 resulting from oxaloacetate transamination in mitochondria (+39%, Fig. 6a; Extended Data Fig. 6 reports the bar graphs of mass isotopomer distribution of all the analysed metabolites; $n = 2$ independent experiments from four pooled mice per genotype per transduction). This result was consistent with the increased levels of total aspartate documented by steady-state metabolomics in *Opa1*^{tg} pre-adipocytes (Fig. 5a). These data indicate that TCA cycle in *Opa1*^{tg} pre-adipocytes can contribute to the biosynthesis of aspartate that supports urea cycle. On the other hand, these flux analyses do not support a key role for TCA cycle-derived fumarate in the 180% fumarate increase observed in Fig. 5a in *Opa1*^{tg} compared to WT pre-adipocytes. The [^{13}C4,^{15}N]-L-aspartic acid flux experiments allowed us to address the relative contribution of urea cycle and purine synthesis on fumarate production. M4 fumarate (that can derive from de novo purine biosynthesis or from urea cycle) increased by 160% in *Opa1*^{tg} pre-adipocytes compared to WT cells. Conversely, the TCA cycle specific M3 fumarate increased by 18% and M1 inosine monophosphate (IMP) labelling decreased by 4% in *Opa1*^{tg} pre-adipocytes, indicating that flux through de novo purine biosynthesis was not enhanced by Opa1, and hence the observed fumarate accumulation was unlikely to be caused by de novo purine biosynthesis derived fumarate (Fig. 6b). Noteworthy, the incorporation of ^{15}N from aspartate into M1 arginine was increased in *Opa1*^{tg} (8%) compared to WT pre-adipocytes, indicating that Opa1 favours nitrogen incorporation from aspartate into urea cycle at the expense of cytoplasmic transamination to glutamate that was conversely decreased (−15%) (Fig. 6b).

To verify formally whether the urea cycle was causally linked to the cytosolic fumarate accumulation, we performed the same

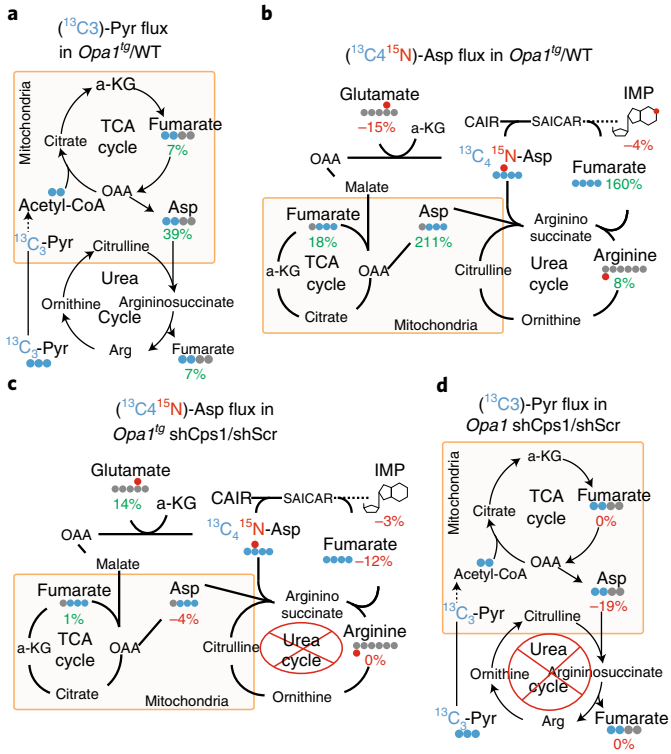

Fig. 6 | Increased urea cycle flux in *Opa1*^{tg} pre-adipocytes. a, Atom tracing of the indicated metabolites from [^{13}C3]-pyruvate in SAT WT and *Opa1*^{tg} pre-adipocytes. Key steps of TCA and urea cycles are indicated. Blue dots represent labelled carbon atoms in the isotopomer. Numbers indicate the percentage variation of the indicated labelled isotopomer in *Opa1*^{tg} versus WT pre-adipocytes (in green when increased, in red if decreased). Data are from two independent LC–MS/MS experiments, each performed on four mice per genotype. **b**, Atom tracing of the indicated metabolites from [^{13}C4,^{15}N]-L-aspartic acid in experiments as in **a**. Labelled carbon atoms are shown as blue dots, labelled nitrogen atoms as red dots in the isotopomer. Numbers indicate the percentage variation of the indicated labelled isotopomer in *Opa1*^{tg} versus WT pre-adipocytes. Data are from two independent LC–MS/MS experiments each performed on four mice per genotype. **c**, Atom tracing experiments as in **b** were performed in SAT *Opa1*^{tg} pre-adipocytes transduced with shRNAs against *Cps1* (shCps1) or a scramble control sequence (shScr). Numbers indicate the percentage variation of the indicated labelled isotopomer in shCps1 versus shScr *Opa1*^{tg} pre-adipocytes. Data are from two independent LC–MS/MS experiments each performed on four mice per transduction condition. **d**, Atom tracing experiments as in **a** were performed in shCps1 or shScr transduced SAT *Opa1*^{tg} pre-adipocytes. Numbers indicate the percentage variation of the indicated labelled isotopomer in shCps1 versus shScr *Opa1*^{tg} pre-adipocytes. Data are from two independent LC–MS/MS experiments each performed on four mice per transduction condition.

tracing experiments in *Opa1*^{tg} pre-adipocytes in which we down-regulated Cps1. Lentiviral delivery of shRNA against Cps1 (ShCps1) in *Opa1*^{tg} pre-adipocytes led to a decrease in [^{13}C3]-pyruvate flux through TCA cycle activity. The increase in mitochondrial M2 fumarate labelling went from 7% to 1% in ShCps1 *Opa1*^{tg} pre-adipocytes (Fig. 6c). The increase in ^{15}N incorporation in M1 arginine from [^{13}C4,^{15}N]-L-aspartic acid dropped from 8% to 0% on Cps1 silencing, confirming the efficient reduction in urea cycle flux (Fig. 6d). Strikingly, following ShCps1 we did not observe any more an increase in M4 fumarate labelling, but a decrease (−12%). Conversely, ^{15}N incorporation to M1 glutamate through cytoplasmic transamination increased by 14% (Fig. 6d). These data indicate that the urea cycle accounts for the fumarate production in *Opa1*^{tg} pre-adipocytes. Altogether, these results unveil a causal link between Opa1-mediated urea cycle activity stimulation and cytoplasmic fumarate production. In this context, the TCA cycle is crucial to supply the urea cycle with aspartate.

Opa1 is required for WAT and BAT maintenance and function. We next wished to verify if adipose tissue-specific *Opa1* deletion impaired brite differentiation of pre-adipocytes by curtailing urea cycle-dependent fumarate accumulation. To this end, we generated fat-specific *Opa1* knockout mice (*Opa1*$^{\Delta AT}$) by crossing adiponectin-Cre (Adipoq-Cre) mice to *Opa1*$^{flx/flx}$ mice[12,49]. Because adiponectin is a downstream target of the master regulator of adipogenesis PPARγ2, our strategy ensures *Opa1* deletion selectively in mature adipocytes. Indeed, BAT and WAT levels of OPA1 were decreased in homo and heterozygous 12-week-old *Opa1*$^{\Delta AT}$ mice (Extended Data Fig. 7a). Although food intake was not significantly different, subcutaneous (SAT) and visceral (VAT) fat depots in *Opa1*$^{\Delta AT}$ mice were significantly decreased (Extended Data Fig. 7b,c), leading to a decrease in fat mass (Extended Data Fig. 7d). Furthermore, histological analysis of the residual WAT of 3-month-old *Opa1*$^{\Delta AT}$ mice revealed a reduced number of adipocytes that were enlarged and dispersed among fibrotic and inflamed tissue (Extended Data Fig. 7e,f). Given these tissue morphology defects, we next sought to address whether *Opa1* loss also affected adipose tissue regulatory functions. Adiponectin is largely produced by adipose tissue and controls whole-body metabolism and disease susceptibility[50]. Levels of secreted adiponectin were greatly decreased in *Opa1*$^{\Delta AT}$ mice; simultaneously, basal levels of insulin were significantly increased (Extended Data Fig. 7g, h). Thus, *Opa1* is required for adipose tissue architecture and endocrine function. However, body weight was not different among *Opa1*$^{\Delta AT}$ mice and their control littermates (WT: 26.96 ± 0.45 g; *Opa1*$^{\Delta AT}$: 25.54 ± 0.84 g, $n = 5$ 12-week-old mice, $P = 0.11$), despite the loss of SAT and VAT in the former, suggesting a lipoatrophic phenotype. Indeed, liver size and lipid accumulation were increased in *Opa1*$^{\Delta AT}$ mice (Extended Data Fig. 7i,j), an indication of abnormal hepatic fat accumulation. *Opa1*$^{\Delta AT}$ mice were also glucose intolerant (Extended Data Fig. 6k) and severely insulin resistant (Extended Data Fig. 7l), indicating that *Opa1* sustains adipocyte function and that its adipose tissue-specific ablation finally results in insulin resistance. We next analysed BAT function in *Opa1*$^{\Delta AT}$ mice. The iBAT was classically brown-red in control mice, whereas it appeared enlarged and cream-coloured in 3-month-old *Opa1*$^{\Delta AT}$ littermates, and histological analysis revealed adipocytes with a mixed white–brown phenotype, characterized by unilocular and multi-locular fat droplets in *Opa1*$^{\Delta AT}$ iBAT (Extended Data Fig. 8a). Consistently, levels of UCP1 (Extended Data Fig. 8b,c) as well as of other brown adipocyte markers and mitochondrial regulators were reduced in *Opa1*$^{\Delta AT}$ iBAT (Extended Data Fig. 8d). Thermogenic activity, measured as the ability to sustain body temperature in response to exposure to 4 °C for 72 h, was reduced in 3-month-old *Opa1*$^{\Delta AT}$ mice (Extended Data Fig. 8e, f). Altogether, these data establish an essential role for Opa1 in the maintenance and function not only of WAT, but also of BAT.

Reduced fumarate levels, browning in *Opa1*$^{\Delta AT}$ pre-adipocytes. We next evaluated whether browning was impaired in vivo in *Opa1*$^{\Delta AT}$ SAT and in vitro in *Opa1*$^{\Delta AT}$ pre-adipocytes. β3-adrenergic stimulation was unable to induce UCP1 or the appearance of BAT-like adipocytes in *Opa1*$^{\Delta AT}$ SAT (Extended Data Fig. 9a, b). Steady-state metabolomics indicated that fumarate levels were reduced in *Opa1*$^{\Delta AT}$ SAT, where MetaboAnalyst showed a reduction in the same pathways, including urea cycle, that were conversely upregulated in *Opa1*^{tg} SAT (Extended Data Fig. 9c, d). We therefore turned to our protocol of in vitro preadipocyte differentiation into brite adipocytes. During brite induction of *Opa1*$^{\Delta AT}$ pre-adipocytes, Opa1

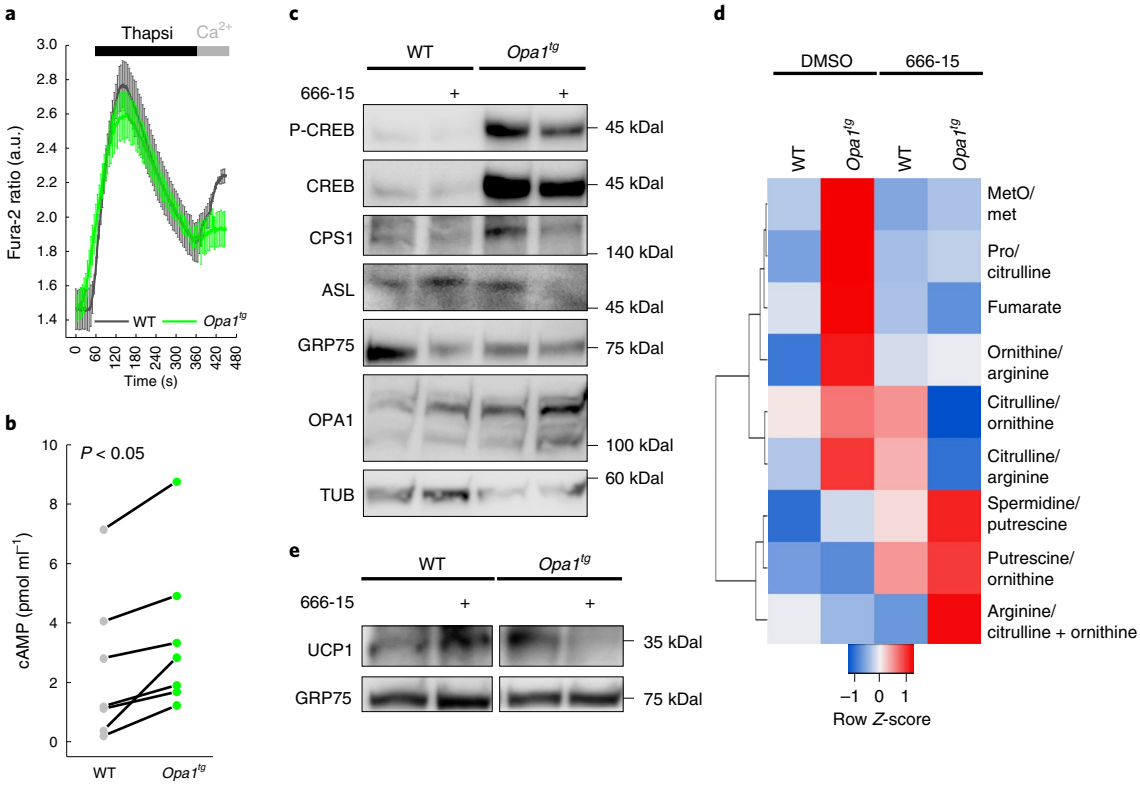

Fig. 7 | Opa1 promotes adipocyte Ucp1 transcription via CREB-mediated urea cycle induction. a, Real-time imaging of Fura-2 fluorescence ratio in WT and *Opa1*^{tg} SAT pre-adipocytes. Where indicated, cells were perfused with 1 µM thapsigargin (thapsi) and 2 mM Ca^{2+}. Data are mean ± s.e.m. of three (WT) to four (*Opa1*^{tg}) independent experiments (n = 7–15 cells imaged per experiment). **b**, Levels of cAMP in pre-adipocytes isolated from mice of the indicated genotype. Each data pair corresponds to a pair of *Opa1*^{tg} and WT littermates (n = 7 per genotype). P = 0.015 in a paired-sample t-test. **c**, Representative immunoblots using the indicated antibodies of equal amounts of protein (20 µg) from WT and *Opa1*^{tg} SAT pre-adipocytes (n = 5 independent experiments). Where indicated, pre-adipocytes were treated with the CREB inhibitor 666-15 (10 µM). **d**, Heat map constructed by hierarchical clustering using Pearson's correlation of metabolite levels in WT and *Opa1*^{tg} SAT pre-adipocytes differentiated into brite adipocytes (n = 2 independent experiments over three mice per genotype). Where indicated, pre-adipocytes were treated with the CREB inhibitor 666-15. **e**, Representative immunoblots using the indicated antibodies of equal amounts of protein (20 µg) from WT and *Opa1*^{tg} SAT pre-adipocytes 5 days following differentiation into brite adipocytes (n = 5 independent experiments).

levels did not increase, as expected. Similarly, Ucp1 expression was also not induced, confirming the brite differentiation defect of these Opa1 knockout cells (Extended Data Fig. 9e). We next addressed by steady-state metabolomics whether fumarate levels were also curtailed during brite differentiation of *Opa1*$^{f/f}$ pre-adipocytes infected with an adenovirus carrying a Cre recombinase, compared to control (green fluorescent protein, GFP) infected *Opa1*$^{f/f}$ pre-adipocytes. Notably, not only fumarate, but also urea cycle intermediates such as Arg, ornithine, spermidine and spermine were reduced during differentiation of Opa1-deficient pre-adipocytes (Extended Data Fig. 9f). Finally, we formally tested whether the defect in brite differentiation of Opa1-deficient pre-adipocytes could be rescued by exogenous fumarate. During brite differentiation of Cre infected *Opa1*$^{f/f}$ pre-adipocytes, DMF could stimulate Ucp1 induction (Extended Data Fig. 9g). Altogether, our data indicate that the impairment in preadipocyte browning due to *Opa1* deletion is accompanied by a reduction in fumarate levels and that *Opa1*$^{\Delta AT}$ preadipocyte browning can be rescued by exogenous fumarate supplementation.

Opa1 engages CREB to drive urea cycle genes transcription. Opa1 can be retrieved in the same complex with the glutamate/aspartate exchanger Slc25a13 (citrin) crucial for the progression of urea cycle, potentially explaining at the molecular level the connection between Opa1 and urea cycle[51]. It was, however, surprising that mild Opa1 overexpression resulted in increased expression of urea cycle enzymes. We reasoned that their coordinated induction could be orchestrated by master transcriptional regulators. Urea cycle genes share common regulatory elements, such as cAMP-response elements (CREs) and glucocorticoid-response elements (GREs)[52,53]. Notably, CREB was predicted as a significant upstream regulator in the brite differentiation of *Opa1*^{tg} white pre-adipocytes (Extended Data Fig. 4b). Multiple signalling pathways with cAMP and calcium-regulated protein kinases can phosphorylate and activate CREB. Gene ontology enrichment analysis revealed that many genes upregulated in *Opa1*^{tg} white pre-adipocytes are significantly associated with cAMP signalling and with ion channels function, suggesting the interesting possibility that Opa1 overexpression could control urea cycle gene expression by modulating calcium ion (Ca^{2+}) levels (Supplementary Table 2)[54]. However, the measured cytosolic Ca^{2+} levels (at baseline or after the discharge of the endoplasmic reticulum stores) were comparable in WT and *Opa1*^{tg} pre-adipocytes. If anything, capacitative Ca^{2+} entry in *Opa1*^{tg} pre-adipocytes was slightly decreased, ruling out the possibility that Opa1 controls expression of urea cycle enzymes by augmenting intracellular Ca^{2+} levels (Fig. 7a). In our metabolomics analysis we were unable to distinguish cAMP from total adenosine monophosphate (AMP) levels that were increased in *Opa1*^{tg} pre-adipocytes (Fig. 7a). Of note, because energy charge [(ATP + 0.5 ADP)/(ATP + ADP + AMP)] was unaffected by Opa1 overexpression (0.033 ± 0.002 in WT pre-adipocytes and 0.0030 ± 0.002 in *Opa1*^{tg}

pre-adipocytes, $n=3$, $P=0.1$ in a non-parametric Kruskal–Wallis analysis of variance (ANOVA)), we postulated that the observed increase in AMP could be due to elevated cAMP. In freshly prepared *Opa1*^{tg} SAT pre-adipocytes cAMP concentrations were indeed always higher than those measured in cells isolated from their age and sex matched WT littermates (Fig. 7b). These data pointed to a possible role for CREB in orchestrating the induction of urea cycle enzymes in *Opa1*^{tg} pre-adipocytes. Indeed, we measured increased CREB phosphorylation (a proxy of CREB activation) in *Opa1*^{tg} pre-adipocytes where CPS1 and ASL levels were also higher (Fig. 7c). To understand if the sustained CREB activity was responsible for the induction of the urea cycle enzymes CPS1 and ASL upregulated in *Opa1*^{tg} pre-adipocytes, we pharmacologically inhibited CREB with the specific inhibitor 666-15[55]. As expected, 666-15 reduced CREB phosphorylation. More importantly, in *Opa1*^{tg} pre-adipocytes treated with 666-15 the expression of CPS1 and ASL was reduced to WT levels (Fig. 7c) (p-CREB/CREB: 2.4 ± 1.1 in dimethylsulfoxide (DMSO) *Opa1*^{tg} versus WT pre-adipocytes, 0.5 ± 0.01 in 666-15 versus DMSO treated *Opa1*^{tg}, $n=6$–3, $P<0.05$; CPS1: 2.3 ± 0.3 in DMSO *Opa1*^{tg} versus WT pre-adipocytes, 0.18 ± 0.1 in 666-15 versus DMSO treated *Opa1*^{tg}, $n=5$–4, $P<0.05$; ASL: 4.5 ± 1.5 in DMSO *Opa1*^{tg} versus WT pre-adipocytes, 0.79 ± 0.06 in 666-15 versus DMSO treated *Opa1*^{tg}, $n=5$–3, $P<0.05$). Steady-state metabolomics indicated that 666-15 reduced the fumarate accumulation typical of *Opa1*^{tg} pre-adipocytes (Fig. 7d). Finally, CREB inhibition reduced browning of *Opa1*^{tg} but not of WT pre-adipocytes (Fig. 7e). Altogether, our data identify that cAMP/CREB links Opa1 to induction of urea cycle enzymes and adipocyte browning.

Lower *KDM3a* and *CPS1* in VAT from patients with obesity. Finally, we verified whether *KDM3a* and the key urea cycle gene *CPS1* were reduced in the visceral adipose tissue from the cohort of obese and matched normal weight individuals studied here. *KDM3A* and *CPS1* expression was lower in these obese patients undergoing bariatric surgery (Extended Data Fig. 10a,b). Interestingly, both *CPS1* and *KDM3a* expression correlated with that of *OPA1* (Extended Data Fig. 10c,d), suggesting that expression of *OPA1*, *CPS1* and *KDM3A* is higher in visceral WAT from leaner individuals, as in mouse *Opa1*^{tg} pre-adipocytes.

Discussion

The relationship between obesity and obesity-related disorders and mitochondrial function and morphology is complex, especially because often the former is dictated by the latter. To delve into this relationship, we investigated the role of mitochondrial morphology in WAT function by combining clinical data, unbiased genomic and metabolomic approaches and genetically modified mouse models. We demonstrate that the mitochondrial cristae shape and fusion protein Opa1 cell-autonomously defines the browning potential of WAT by impinging on urea cycle and on the Jumanji family histone demethylase Kdm3a.

Genetic analyses of cohorts of rare obesity-discordant monozygotic twins implicated adipose tissue mitochondrial dysfunction in the development of obesity[23,56]. However, 'mitochondrial dysfunction' is too broad a concept to provide insights into the adipose tissue differences between lean individuals and patients with obesity. Conversely, because mitochondrial function often follows form, the use of conditional knockout mouse models for the mitochondrial fusion and endoplasmic reticulum tethering protein Mfn2 in the adipose tissue revealed its importance in thermogenic function of BAT, as well as its role in WAT expandability[18,19]. While these studies substantiate the importance of mitochondrial morphology in adipose tissue biology, they fall short of clarifying whether and how, for example, Mfn2 is involved in human obesity. To overcome this issue, we decided to take an unbiased approach and inspect levels of mitochondria-shaping proteins in defined cohorts of clinically characterized individuals with obesity. Besides the significant reduction of *OPA1* levels in human obesity before clinically observed complications, our attention was caught by the negative correlation between *OPA1* levels and indices of obesity comorbidity. This correlation suggested a key role for *OPA1* in the function of adipocytes and higher levels of *OPA1* might favour adipose tissue function by capitalizing on a mouse model of mild Opa1 overexpression. Interestingly, the remodelling of adipose tissue in lean and obese states is favoured in these *Opa1*^{tg} mice: fat depots and body weight are reduced on a standard diet, while on HFD the ability of adipose tissue to expand is enhanced. All in all, the Opa1-dependent plasticity of adipose tissue results in improved glucose metabolism and insulin sensitivity. In addition to the ability of WAT to expand, BAT can directly contribute, on stimulation, to the control of body mass and adiposity by expending extra energy as heat. In *Opa1*^{tg} mice adaptative thermogenesis is enhanced after feeding a HFD, on acute cold exposure or adrenergic stimulation, with the appearance of brite cells in SAT and even in VAT. This remarkable result implies that Opa1 facilitates the transition of white to brown adipocytes and prompted us to exploit this property of *Opa1*^{tg} white pre-adipocytes to elucidate the molecular pathways linking mitochondria and white to brite transition.

By investigating the differentiation of primary *Opa1*^{tg} white pre-adipocytes we reveal a browning pathway in which *Ucp1* transcription is mediated by KDM3a, a member of the Jumanji demethylases family also known as Jhdm2a or Jmjd1a. KDM3a promotes *Ucp1* expression by decreasing H3K9 demethylation and facilitating the recruitment of PPARγ and PGC1α on the *Ucp1* promoter[41]. Interestingly, differences in DNA methylation characterize subcutaneous WAT of monozygotic twins discordant for T2DM[57]. Because in metabolically healthy monozygotic obesity-discordant twin pairs *OPA1* levels are reduced together with those of *KDM3a*, a potential link between methylation and mitochondrial function might exist *tout court* in obesity.

To understand how OPA1 stimulates *Kdm3a* transcription we integrated transcriptional, metabolomic and fluxomic data, revealing that the accumulation of fumarate, which is per se able to induce *Kdm3a*-dependent adipocyte *Ucp1* transcription, was a consequence of OPA1 stimulation of urea cycle. Genetic and labelled metabolite flux experiments indeed highlight that the key urea cycle enzyme Cps1 is required for Opa1-induced fumarate accumulation and pre-adipocyte browning, unveiling the mechanism by which Opa1 can sustain brite differentiation of adipocytes. Urea cycle is normally believed to be confined in the liver and in enterocytes. However, its enzymes are also found in adipose tissue[58], higher urea levels are a signature of BAT[59] and adipose tissue levels of *CPS1* correlate with weight maintenance in genome-wide association studies performed within the Diogenes weight loss study[60]. Finally, the urea cycle intermediate arginine that also accumulates in *Opa1*^{tg} adipocytes can increase BAT activity[61]. Altogether, stimulation of the urea cycle emerges as an appealing strategy to promote browning of WAT. How the urea cycle is transcriptionally regulated in non-hepatic cells is largely unknown. In *Opa1*-overexpressing preadipocyte levels of the key second messenger cAMP is higher. In adipose tissue cAMP activates lipolysis, glucose uptake and thermogenesis, enhancing β3-AR signalling via CREB activation. Interestingly, our analysis extends the list of CREB target genes in the adipose tissue to the rate limiting urea cycle enzyme Cps1. It would be interesting to understand whether Cps1 is a required component of the β3-agonist induced brownization.

Whether the metabolic function of Opa1 reported here depends on its ability to promote mitochondrial fusion or on its distinguishable roles in mitochondrial biology and metabolism must still be addressed. We contend that this metabolic Opa1 function is likely to be independent from its pro-fusion role for two main reasons: first, we did not find an association between levels of the two other

mitochondrial fusion genes *MFN1* and *MFN2* and metabolic health in the analysed cohorts. Second, Opa1 overexpression stimulates pyruvate flux through TCA in adipocytes, a result resonating with the ability of Opa1 to promote mitochondrial respiration that requires TCA-derived reducing equivalents and that is independent from mitochondrial fusion[12]. A second interesting question is how Opa1 controls cAMP levels. While we ruled out Ca^{2+} as an effector, increased cAMP levels can result from reduced phosphodiesterases or increased adenylate cyclase activity. Interestingly, DMF can activate adenylate cyclase in other cell types[62], raising the possibility that fumarate is at the centre of a feed-forward loop in which its initial accumulation boosts urea cycle by the cAMP–CREB axis.

Because adipose tissue levels of *OPA1*, *KDM3A* and *CPS1* are reduced in the studied cohorts of individuals with obesity, our work nominates adipose tissue urea cycle reactivation as a strategy to increase tissue plasticity and perhaps counteract obesity.

Methods

Human subjects. This study included 26 obesity-discordant monozygotic pairs (within-pair difference of BMI $\geq$3 kg m^{-2})[63]. Written informed consent was obtained from all participants. The study protocols were approved by the Ethical Committee of the Helsinki University Central Hospital. Biopsies of periumbilical SAT were obtained under local lidocaine anaesthesia by a surgical technique and snap frozen in liquid nitrogen for the extraction of total RNA as described[56]. Transcriptomics experiments were performed with Affymetrix U133 Plus 2.0 chips[56].

Adipose tissue biopsies of intra-abdominal fat (VAT) were obtained from three different groups of human subjects classified based on clinical evaluation in lean controls, normoglycaemic patients with obesity (obese) and patients with obesity and diabetes (obese-T2DM). A short description of patients is found in Supplementary Table 2. The study was approved by the Ethical Committee of Padua Hospital (Protocol 2892P, 10 June 2013) and each subject gave informed written consent. Total RNA was extracted from abdominal fat biopsy samples and analysed by quantitative real-time PCR for selected genes. Primers are listed in Supplementary Table 3.

Mouse studies. Animal housing and all the experimental procedures were authorized by the Italian Ministry of Health (approved protocol: 383-2015-PR to L.S.). Mice were housed five per cage in a temperature (22–24 °C) and humidity-controlled (50%) colony room, maintained on a 12 h light/dark cycle (07:00 to 19:00 light on), with standard food (Mucedola 4RF21 standard diet) and freely available water and environmental enrichments.

Opa1^{tg} mice are described[12,26]. To generate constitutive adipose-specific Opa1 knockout mice (*Opa1*$^{\Delta AT}$), *Opa1*$^{f/f}$ animals[12] were crossed with transgenic mice expressing Cre under the control of the adiponectin promoter (Adipoq-Cre, JAX no. 010803) and kept in a heterozygous breeding scheme. Cre^{-} littermates were used as controls. PCR genotyping was performed with the following primers: Opa1 Fw: 5'-CAGTGTTGATGACAGCTCAG-3' and Opa1 Rv: 5'-CATCACACACTAGCTTACATTTGC-3'; Cre Fw 5'-GGATGTGCCATGTGAGTCTG-3' and Cre Rv 5'-ACGGACAGAAGCATTTTCCA-3'.

In vivo mouse treatments. Mice were fed with a HFD (Rodent Diet with 60% kcal% fat, Research Diets, Inc. D12492) for 9 weeks beginning at 12 weeks of age. Body weight was recorded weekly. For acute cold studies, mice were transferred from standard housing condition to 4 °C and maintained at 4 °C for 3 days. For all cold studies mice had free access to food and water. Body skin temperature was measured at the indicated time points, using FLIR T450sc thermal imaging camera (FLIR Systems Inc.). CL 316,243 hydrate (disodium 5-[(2R)-2-[[(2R)-2-(3-chlorophenyl)-2-hydroxyethyl]amino]propyl]-1,3-benzodioxole-2,2-dicarboxylate hydrate, Sigma-Aldrich C5976) at a dose of 1 mg kg^{-1} was administered through an i.p. injection every day for 5 days.

Enclosed metabolic chambers with digital oxygen (O_2), carbon dioxide (CO_2), food and water intake sensors (TSE Systems) were used for WT and *Opa1*^{tg} mice simultaneously to measure energy expenditure, physical activity, indirect calorimetry and food/water intake. The experiment was performed in standard housing conditions and on cold exposure (18 °C).

Whole-body composition was measured using nuclear MRI (EchoMRI-100H Body Composition Analyzer, EchoMRI LLC) in restrained, conscious mice.

Measurement of serum hormones. Blood was collected by cardiac puncture immediately after killing and was kept at RT for 30 min to let blood clot for serum isolation. Clotted blood was then centrifuged at 3,000*g* for 15 min at 4 °C and the serum was transferred in a separate tube. Insulin, leptin, adiponectin were measured using the following kits: Adiponectin enzyme-linked immunosorbent assay (ELISA) (Millipore EZMADP-60K); Leptin ELISA (Millipore EZML-82K); Insulin ELISA (Millipore EZRMI-13K).

Glucose tolerance test. Mice were fasted for 12 h before any glucose tolerance test. Basal blood glucose was sampled before glucose administration by i.p. injection at a dose of 2 mg kg^{-1}. Blood samples were taken at the indicated time intervals from tail blood using a glucometer (FreeStyle).

Insulin sensitivity test. Insulin sensitivity was assessed by injecting mice that had been fasted for 5 h with free access to water, intraperitoneally with 1 unit per kg insulin (Humulin R 100UI/ML, Eli Lilly and Company). Blood glucose was measured before the injection with insulin and at the indicated time intervals from tail blood using a glucometer (FreeStyle).

Mouse primary adipocytes. Mouse primary white pre-adipocytes were isolated as described[64] and were induced to differentiate with adipogenic medium containing 66 nM insulin, 100 nM dexamethasone (Sigma-Aldrich D4902), 1 nM 3,3′,5-triiodo-L-thyronine (Sigma-Aldrich T2877), 0.25 mM 3-isobutyl-1-methylxanthine (IBMX, Sigma-Aldrich I5879), 10 µM rosiglitazone maleate (AdooQ Bioscience A10809) in 5% fetal bovine serum. IBMX and rosiglitazone were removed after 3 days of culture. For white to brown differentiation, the adipogenic medium was supplemented with 10 µM rosiglitazone and 1 µM norepinephrine (R + NE) and maintained for 7 days. Where indicated pre-adipocytes were treated for 24 h with the CREB Inhibitor 666-15 (Millipore Sigma 5383410001).

RNA isolation and gene expression analyses. Total RNA was prepared from adipose tissue using trizol (Invitrogen 15596-018). Total RNA was purified from primary cells using the RNeasy Mini Kit (Qiagen 74106). RNA was quantified by spectrophotometry using Nanodrop One (ThermoFisher), and purity was assessed by the absorbance ratios of 260:280 and 260:230 nm. From an equal amount of total RNA of each sample, complementary DNA was generated with GoScript Reverse Transcription System (Promega A5001). Real-time qPCR based on the SYBR Green chemistry (GoTaq qPCR Master Mix Promega A6002) was carried out using the QuantStudio 5 Real-Time PCR System (Thermo Fisher). The designed primer sequences are in Supplementary Table 3. The housekeeping genes β-actin and S18 were used as internal controls for cDNA quantification and normalization. Relative changes in gene expression were determined by the $2^{(-\Delta\Delta C(T))}$ method or by the relative standard curve method. Data are presented as expression fold change normalized for gene expression.

Histology and immunofluorescence. Adipose tissue samples were fixed overnight at 4 °C in 4% paraformaldehyde (PFA) and then dehydrated through serial ethanol concentrations for paraffin embedding. Paraffin-embedded tissues were used for Mayer's haematoxylin and eosin (H&E) staining. Analysis of adipocytes size was performed on H&E-stained 8-µm-thick sections using ImageJ on four samples per genotype (approximately 1,000 adipocytes per sample). Livers were fixed in 1% PFA in phosphate-buffered saline (PBS) at RT for 15 min, equilibrated in a sucrose gradient, frozen in liquid nitrogen, sectioned, and processed for histological analyses. Sections were obtained with a cryostat (Leica CM1850, Leica Microsystems). Oil Red O (Polysciences, Inc. 06317) staining of frozen sections was performed using 60% isopropanol saturated with Oil Red O dye for 1 h at RT.

For ultrastructural studies, adipose tissue was fixed in 2% PFA and 2.5% glutaraldehyde in 0.1 M sodium cacodylate pH 7.4. Electron microscopies were acquired as described.

For immunofluorescence staining paraffin-embedded sections of BAT were deparaffinized, rehydrated and, after heat-mediated antigen retrieval with citrate buffer pH 6, were blocked with Donkey Serum (Merck D9663). Sections were incubated with 1:200 anti-UCP1 overnight at 4 °C followed by Donkey anti-Rabbit IgG (H + L) Secondary antibody Alexa Fluor 594 (ThermoFisher A-21207; 1:200). Nuclei were counterstained with 4.6-diamidino-2-phenylindole (DAPI) (Merck F6057). Images were captured using AF6000 microscope and LAS AF software 4.0 (Leica Microsystems GmbH).

RNA sequencing. Total RNA was extracted using RNeasy Mini Kit (Qiagen) following supplier's instructions. The quality of extracted RNAs, in terms of integrity and lack of protein/carbohydrate contamination was assessed with an Agilent 2100 Bioanalyzer instrument (Agilent Technologies) and a Nanodrop 2000 spectrophotometer. After the confirmation of the high integrity (RIN >9) and lack of significant contamination, RNAs were processed with a QuantSeq 3' mRNA-Seq Library Prep Kit FWD (Lexogen) to produce 3' end-enriched sequencing libraries compatible with Illumina sequencing, according to the manufacturer's instructions. Barcoded libraries were pooled and sequenced at the Oklahoma Medical Research Foundation NGS Core centre on a single lane of an Illumina NextSeq 500 using a v2 kit, run on mid-output settings with 150 sequencing cycles (single end).

Raw sequencing outputs were demultiplexed, imported in the CLC Genomics Workbench v10 (Qiagen), and trimmed based on base-calling quality (threshold of 0.05), presence of residual sequencing adaptors, poly-A and poly-G stretches, the latter resulting from 'no-signal' from the two-colour chemistry used by

NextSeq platforms. Resulting trimmed reads shorter than 75 nucleotides were also discarded before further analysis.

Clean reads were mapped on the reference annotated mouse genome assembly GRCm38 version from Ensembl, using the RNA-seq mapping tool embedded in the CLC Genomics Workbench package, with length and similarity fraction parameters set to 0.75 and 0.98, respectively. Unique exon read counts were normalized by totals (assuming a total of 1 million reads per sample), de facto obtaining transcript per million expression values, due to the lack of representation bias due to the length of mRNA molecules, enabled using 3' end-enriched libraries.

Normalized gene expression values were compared between R + NE-treated and untreated adipocytes with a Kal's *Z*-test to identify differentially expressed genes based on fold change cut-off of 2 and a false discovery rate (FDR)-corrected *P* value of less than 0.05. Gene IDs, fold change and FDR values for DEGs were then exported to IPA and evaluated with a core analysis to identify altered canonical pathways and predict upstream regulators and downstream effects, providing the framework for the construction of a network of gene regulation supported by literature data, which was manually edited to include new experimental data provided by the present study.

Western blotting. Protein lysates were prepared from homogenized adipose tissues or cells and lysed in RIPA buffer supplemented with protease inhibitors (PIC, Sigma). Protein lysates were clarified to eliminate the extremely high lipid content by several centrifugation steps (4 °C, 20 min, 12,000*g*). Protein concentration was determined using Pierce BCA Protein Assay Kit (ThermoFisher 23225). Gel sample buffer (Invitrogen) supplemented with 1 mM dithiothreitol was added to the samples, which were then boiled, separated on gels (Invitrogen), and transferred to polyvinylidene difluoride (PVDF) membranes (Immobilon P, Millipore). Membranes were then probed with the following antibodies as indicated in the figure legends: OPA1 (BD Biosciences 612607, 1:1,000); UCP1 (Sigma-Aldrich U6382, 1:1,000); GRP75 (H-155, Santa Cruz Biotechnology sc-13967, 1:1,000); ACTIN (Merk Millipore MAB1501, 1:10,000); TUBULIN (Santa Cruz Biotechnology 5286, 1:10,000); CREB (Cell Signaling Technology 9197S, 1:1,000); Phospho-CREB (Cell Signaling Technology 9198S, 1:1,000); CPS1 (Sigma-Aldrich HPA021400, 1:1,000); ASL (Santa Cruz Biotechnology sc-166787, 1:1,000).

Retrovirus production. Retroviral shKdm3a and shScramble constructs were a gift from F. Fuks. For the generation of retrovirus supernatants, platinum-E packaging cells were seeded 1 day before transfection. Cells were transfected the next day at 70% confluency using PEI (Polysciences). Supernatant was collected 24, 48 and 72 h after transfection and filtered with a 0.45-mm PVDF filter (Millipore). Polybrene (4 μg ml^{-1}) was added to the viral supernatants and used to infect pre-adipocytes.

Lentivirus production. Three individual MISSION shRNA clones for each target gene were used to find the highest level of knockdown. The following shRNA were used: pLKO.1-shCps1#1 (Sigma-Aldrich TRCN0000252869); pLKO.1-shCps1#2 (Sigma-Aldrich TRCN0000267448); pLKO.1-shCps1#3 (Sigma-Aldrich TRCN0000252866); pLKO.1-shAsl#1 (Sigma-Aldrich TRCN0000120118); pLKO.1-shAsl#2 (Sigma-Aldrich TRCN0000120119); pLKO.1-shAsl#3 (Sigma-Aldrich TRCN0000120117); pLKO.1-shHif1a#1 (Sigma-Aldrich TRCN0000232222); pLKO.1-shHif1a#2 (Sigma-Aldrich TRCN0000054451); pLKO.1-shHif1a#3 (Sigma-Aldrich TRCN0000054449); pLKO.1-puro non-target shRNA (Sigma-Aldrich SHC016). To produce lentiviral particles, HEK 293 T cells were seeded 1 day before transfection. Cell were cotransfected the next day at 70% confluency using PEI (Polysciences, Inc. 23966) with each lentiviral-based transfer vector and lentivirus packaging (psPAX2, Addgene 12260) and envelope plasmids (pMD2-VSVG, Addgene 12259). Supernatant was collected 24, 48 and 72 h after transfection and filtered with a 0.45-mm PVDF filter (Millipore). Polybrene (4 μg ml^{-1}) was added to the viral supernatants and used to infect pre-adipocytes.

Metabolite extraction and LC–MS/MS analysis. Pre-adipocytes isolated from SAT of *Opa1*^{tg} and control mice were grown in six-well plates, harvested in ice-cold PBS and centrifuged at 2,500*g* for 3 min at 4 °C. Pellets were resuspended in 250 μl methanol/acetonitrile 1:1 with 1 ng μl^{-1} [U-$^{13}C_6$]-glucose (internal standard, Sigma-Aldrich, 389374), lysed using a TissueLyser II (Qiagen) and centrifuged (20,000*g* for 5 min, 4 °C). Mature adipocytes isolated from SAT of *Opa1*^{tg}, *Opa1*$^{\Delta AT}$ and the relative control mice were resuspended and lysed as above. Supernatants were filtered through regenerated cellulose, dried and resuspended in methanol (MeOH) (100 μl). Prior derivatization was performed to allow amino acids quantification. To this end, we added 50 μl of a 5% phenyl isothiocyanate in 31.5% ethanol (EtOH) and 31.5% pyridine solution to each sample (10 μl). After 20 min incubation (RT), we dried samples by fluxing N_2 and resuspended them in 100 μl of a 5 mM ammonium acetate in MeOH/water (H_2O) (1:1) solution. We acquired metabolomic data using an API-4000 triple quadrupole mass spectrometer (AB Sciex) coupled with a high-performance liquid chromatography system (Agilent) and CTC PAL HTS autosampler (PAL System). We confirmed the identity of metabolites using pure standards. We quantified metabolites by liquid chromatography–tandem mass spectrometry (LC–MS/MS) using a C18 column (Biocrates) for amino acids and cyano-phase LUNA column (50 mm × 4.6 mm, 5 μm; Phenomenex) for all other metabolites. Samples were analysed in a 10 min run in positive (amino acids) and 5 min run in negative (all other metabolites) ion mode with a 20 multiple reaction monitoring (MRM) transition in positive ion mode and 30 MRM transition in negative ion mode. For positive ion mode analysis, the mobile phases were, phase A: 0.2% formic acid in H_2O; phase B: 0.2% formic acid in acetonitrile. The gradient was T_0: 100% phase A; $T_{5.5\,min}$: 5% phase A, $T_{7\,min}$: 100% phase A with a flow rate of 500 μl min^{-1}. For negative ion mode analysis, the mobile phase was phase A: 5 mM ammonium acetate pH 7 in MeOH. The gradient was 100%A; flow rate was 500 μl min^{-1}. Data analysis and peak review of chromatograms were performed using MultiQuant (v.3.0.2). Quantification of metabolites was based on calibration curves with pure standards. Data were normalized for total protein content calculated by Bradford.

Metabolic tracing analyses. Pre-adipocytes isolated from *Opa1*^{tg} and WT SAT were grown in six-well plates and exposed for 24 h to 0.05 mM [^{13}C4,^{15}N]-L-aspartic acid or 0.5 mM [^{13}C3]-pyruvate. Cells were harvested in ice-cold PBS and centrifuged (500*g*, 3 min, 4 °C). Pellets were resuspended in 250 μl methanol/acetonitrile 1:1 and centrifuged (20,000*g*, 5 min, 4 °C). Supernatants were filtered through regenerated cellulose, dried under N_2 flow, and resuspended in MeOH (100 μl). Metabolomic data were acquired, analysed and reviewed as described above. Samples were analysed after 24 h of labelling to ensure isotopic equilibrium. Methanolic samples were analysed by a 5 min run in negative ion mode. The mobile phases for negative ion mode analysis were phase A: 2 mM ammonium acetate in MeOH; phase B: water. The gradient was 90%A with a flow rate of 500 μl min^{-1}. We corrected detected labelled metabolites for their natural isotope abundance.

Fumarate assay. Forty mg of SAT of *Opa1*^{tg} and WT mice were isolated and rapidly homogenized in 100 μl of fumarate assay buffer; 25 μl of each lysate sample was used for the quantification of fumarate using the fumarate assay kit (Sigma-Aldrich MAK060) according to the manufacturer's instructions.

cAMP assay. WT and Opa1^{tg} white pre-adipocytes were isolated the day before the assay; the same number of cells for each sample was seeded. The following day cells were subjected to 1 h of serum starvation before processing for cAMP analysis using the cAMP complete ELISA kit (Abnova KA0320); 100 μl of each lysate sample was used for the quantification of cAMP according to the manufacturer's protocol.

Calcium imaging. WT and Opa1^{tg} white pre-adipocytes were isolated one day before the assay. The following day cells were incubated at 37 °C in physiological solution (135 mM NaCl, 5 mM KCl, 0.4 mM KH_2PO_4, 1 mM $MgSO_4 \times 7\,H_2O$, 20 mM HEPES, 1 mM Ca^{2+}, 0.1% glucose; pH 7.4 at 37 °C) containing 2 μM Fura-2 (Molecular Probes), 0.04% pluronic acid and 250 μM sulfinpyrazone. After 45 min cells were washed with physiological solution and subsequently the fluorescence intensity was monitored in the presence of 200 μM EGTA. After 30 s, thapsigargin was added, followed by a pulse of 2 mM calcium.

Statistical analyses. Data are presented as mean ± s.e.m. in time course experiments or as box-dot plots in other graphs. In dot-box plots, dots represent the individual measurements, boxes represent the mean ± s.e.m. and whiskers the 10th and 90th percentiles. Dot-box plots margins are specified in each figure legend. Normal distribution of data in each sample where individual measurements were greater than 30 was verified by a Shapiro–Wilk test. If data were not normally distributed, a non-parametric Mann–Whitney *U*-test or Kruskal–Wallis test was used to analyse significance; otherwise, the appropriate parametric *t*-test or ANOVA were used, as specified in the figure legends. If the numerosity of the sample was less than 30, we always used the non-parametric tests specified in the figure legends. A $P \leq 0.05$ was the cut-off for significance.

The discordant twin-pair differential expression analysis of the key regulators of mitochondrial morphology was performed using the limma R package[65]. Specifically, a moderated paired *t*-test which allows for sib-pair effects in the linear model adjusted for for age, sex and smoking was used. The Benjamini and Hochberg (BH) method was applied to control for the FDR, and all the reported significant *P* values survived the BH significance threshold of 0.05 or less. Associations in twin individuals and twin pairs between the expression of mitochondrial fusion and fission genes and clinical traits were assessed using linear-mixed and linear models, respectively, adjusted for age, sex and smoking (package lm and lmer in R)[66]. Both models were adjusted for age, sex and smoking and additionally for twinship in the individual's analysis. Individual associations are analysed treating every subject as an individual; within-pair associations are calculated for heavy–lean co-twin differences of each variable. Nominal *P* values are reported in the figures.

References

1. Apovian, C. M. & Riffenburg, K. M. Perspectives on the global obesity epidemic. *Curr. Opin. Endocrinol., Diabetes, Obes.* **24**, 307–309 (2017).
2. Vegiopoulos, A., Rohm, M. & Herzig, S. Adipose tissue: between the extremes. *EMBO J.* **36**, 1999–2017 (2017).
3. Kershaw, E. E. & Flier, J. S. Adipose tissue as an endocrine organ. *J. Clin. Endocrinol. Metab.* **89**, 2548–2556 (2004).
4. Gesta, S., Tseng, Y. H. & Kahn, C. R. Developmental origin of fat: tracking obesity to its source. *Cell* **131**, 242–256 (2007).
5. Cypess, A. M. et al. Identification and importance of brown adipose tissue in adult humans. *N. Engl. J. Med.* **360**, 1509–1517 (2009).
6. Petrovic, N. et al. Chronic peroxisome proliferator-activated receptor gamma (PPARgamma) activation of epididymally derived white adipocyte cultures reveals a population of thermogenically competent, UCP1-containing adipocytes molecularly distinct from classic brown adipocytes. *J. Biol. Chem.* **285**, 7153–7164 (2010).
7. Wu, J. et al. Beige adipocytes are a distinct type of thermogenic fat cell in mouse and human. *Cell* **150**, 366–376 (2012).
8. Bostrom, P. et al. A PGC1-alpha-dependent myokine that drives brown-fat-like development of white fat and thermogenesis. *Nature* **481**, 463–468 (2012).
9. Wu, J., Cohen, P. & Spiegelman, B. M. Adaptive thermogenesis in adipocytes: is beige the new brown? *Genes Dev.* **27**, 234–250 (2013).
10. Kusminski, C. M. et al. MitoNEET-driven alterations in adipocyte mitochondrial activity reveal a crucial adaptive process that preserves insulin sensitivity in obesity. *Nat. Med.* **18**, 1539–1549 (2012).
11. Dahlman, I. et al. Downregulation of electron transport chain genes in visceral adipose tissue in type 2 diabetes independent of obesity and possibly involving tumor necrosis factor-alpha. *Diabetes* **55**, 1792–1799 (2006).
12. Cogliati, S. et al. Mitochondrial cristae shape determines respiratory chain supercomplexes assembly and respiratory efficiency. *Cell* **155**, 160–171 (2013).
13. Gomes, L. C., Di, B. G. & Scorrano, L. During autophagy mitochondria elongate, are spared from degradation and sustain cell viability. *Nat. Cell Biol.* **13**, 589–598 (2011).
14. Bach, D. et al. Expression of Mfn2, the Charcot–Marie–Tooth neuropathy type 2A gene, in human skeletal muscle: effects of type 2 diabetes, obesity, weight loss, and the regulatory role of tumor necrosis factor alpha and interleukin-6. *Diabetes* **54**, 2685–2693 (2005).
15. Toledo, F. G., Watkins, S. & Kelley, D. E. Changes induced by physical activity and weight loss in the morphology of intermyofibrillar mitochondria in obese men and women. *J. Clin. Endocrinol. Metab.* **91**, 3224–3227 (2006).
16. Schneeberger, M. et al. Mitofusin 2 in POMC neurons connects er stress with leptin resistance and energy imbalance. *Cell* **155**, 172–187 (2013).
17. Giacomello, M., Pyakurel, A., Glytsou, C. & Scorrano, L. The cell biology of mitochondrial membrane dynamics. *Nat. Rev. Mol. Cell Biol.* **21**, 204–224 (2020).
18. Boutant, M. et al. Mfn2 is critical for brown adipose tissue thermogenic function. *EMBO J.* **36**, 1543–1558 (2017).
19. Mahdaviani, K. et al. Mfn2 deletion in brown adipose tissue protects from insulin resistance and impairs thermogenesis. *EMBO Rep.* **18**, 1123–1138 (2017).
20. Alavi, M. V. et al. Subtle neurological and metabolic abnormalities in an Opa1 mouse model of autosomal dominant optic atrophy. *Exp. Neurol.* **220**, 404–409 (2009).
21. Pereira, R. O. et al. OPA1 deletion in brown adipose tissue improves thermoregulation and systemic metabolism via FGF21. *eLife* https://doi.org/10.7554/eLife.66519 (2021).
22. Benador, I. Y. et al. Mitochondria bound to lipid droplets have unique bioenergetics, composition, and dynamics that support lipid droplet expansion. *Cell Metab.* **27**, 869–885.e866 (2018).
23. Pietilainen, K. H. et al. Global transcript profiles of fat in monozygotic twins discordant for BMI: pathways behind acquired obesity. *PLoS Med.* **5**, e51 (2008).
24. Heinonen, S. et al. Mitochondria-related transcriptional signature is downregulated in adipocytes in obesity: a study of young healthy MZ twins. *Diabetologia* **60**, 169–181 (2017).
25. Hocking, S., Samocha-Bonet, D., Milner, K. L., Greenfield, J. R. & Chisholm, D. J. Adiposity and insulin resistance in humans: the role of the different tissue and cellular lipid depots. *Endocr. Rev.* **34**, 463–500 (2013).
26. Varanita, T. et al. The OPA1-dependent mitochondrial cristae remodeling pathway controls atrophic, apoptotic, and ischemic tissue damage. *Cell Metab.* **21**, 834–844 (2015).
27. Maffei, M. et al. Leptin levels in human and rodent: measurement of plasma leptin and ob RNA in obese and weight-reduced subjects. *Nat. Med.* **1**, 1155–1161 (1995).
28. Stern, J. H., Rutkowski, J. M. & Scherer, P. E. Adiponectin, leptin, and fatty acids in the maintenance of metabolic homeostasis through adipose tissue crosstalk. *Cell Metab.* **23**, 770–784 (2016).
29. Lowell, B. B. & Spiegelman, B. M. Towards a molecular understanding of adaptive thermogenesis. *Nature* **404**, 652–660 (2000).
30. Tschöp, M. H. et al. A guide to analysis of mouse energy metabolism. *Nat. Methods* **9**, 57–63 (2011).
31. Kalinovich, A. V., de Jong, J. M., Cannon, B. & Nedergaard, J. UCP1 in adipose tissues: two steps to full browning. *Biochimie* **134**, 127–137 (2017).
32. Deveaud, C., Beauvoit, B., Salin, B., Schaeffer, J. & Rigoulet, M. Regional differences in oxidative capacity of rat white adipose tissue are linked to the mitochondrial content of mature adipocytes. *Mol. Cell. Biochem.* **267**, 157–166 (2004).
33. Kim, J. B. et al. Identification of a novel anti-apoptotic E3 ubiquitin ligase that ubiquitinates antagonists of inhibitor of apoptosis proteins SMAC, HtrA2, and ARTS. *J. Biol. Chem.* **288**, 12014–12021 (2013).
34. Harriman, G. et al. Acetyl-CoA carboxylase inhibition by ND-630 reduces hepatic steatosis, improves insulin sensitivity, and modulates dyslipidemia in rats. *Proc. Natl Acad. Sci. USA* **113**, E1796–E1805 (2016).
35. Soni, K. G. et al. Carboxylesterase 3 (EC 3.1.1.1) is a major adipocyte lipase. *J. Biol. Chem.* **279**, 40683–40689 (2004).
36. Jønson, L. et al. Molecular composition of IMP1 ribonucleoprotein granules. *Mol. Cell Proteom.* **6**, 798–811 (2007).
37. Kiyomitsu, T. & Cheeseman, I. M. Cortical dynein and asymmetric membrane elongation coordinately position the spindle in anaphase. *Cell* **154**, 391–402 (2013).
38. Cho, Y., Hazen, B. C., Russell, A. P. & Kralli, A. Peroxisome proliferator-activated receptor γ coactivator 1 (PGC-1)- and estrogen-related receptor (ERR)-induced regulator in muscle 1 (Perm1) is a tissue-specific regulator of oxidative capacity in skeletal muscle cells. *J. Biol. Chem.* **288**, 25207–25218 (2013).
39. Stroud, D. A. et al. Accessory subunits are integral for assembly and function of human mitochondrial complex I. *Nature* **538**, 123–126 (2016).
40. Wang, Q. et al. The hepatokine Tsukushi gates energy expenditure via brown fat sympathetic innervation. *Nat. Metab.* **1**, 251–260 (2019).
41. Abe, Y. et al. Histone demethylase JMJD1A coordinates acute and chronic adaptation to cold stress via thermogenic phospho-switch. *Nat. Commun.* **9**, 1566 (2018).
42. Abe, Y. et al. JMJD1A is a signal-sensing scaffold that regulates acute chromatin dynamics via SWI/SNF association for thermogenesis. *Nat. Commun.* **6**, 7052 (2015).
43. Wellmann, S. et al. Hypoxia upregulates the histone demethylase JMJD1A via HIF-1. *Biochem. Biophys. Res. Commun.* **372**, 892–897 (2008).
44. Kvietikova, I., Wenger, R. H., Marti, H. H. & Gassmann, M. The transcription factors ATF-1 and CREB-1 bind constitutively to the hypoxia-inducible factor-1 (HIF-1) DNA recognition site. *Nucleic Acids Res.* **23**, 4542–4550 (1995).
45. Doe, M. R., Ascano, J. M., Kaur, M. & Cole, M. D. Myc posttranscriptionally induces HIF1 protein and target gene expression in normal and cancer cells. *Cancer Res.* **72**, 949–957 (2012).
46. Aryee, D. N. et al. Hypoxia modulates EWS-FLI1 transcriptional signature and enhances the malignant properties of Ewing's sarcoma cells in vitro. *Cancer Res.* **70**, 4015–4023 (2010).
47. Chandel, N. S. Evolution of mitochondria as signaling organelles. *Cell Metab.* **22**, 204–206 (2015).
48. Lee, J. S. et al. Urea Cycle dysregulation generates clinically relevant genomic and biochemical signatures. *Cell* **174**, 1559–1570.e1522 (2018).
49. Eguchi, J. et al. Transcriptional control of adipose lipid handling by IRF4. *Cell Metab.* **13**, 249–259 (2011).
50. Matsuzawa, Y., Funahashi, T., Kihara, S. & Shimomura, I. Adiponectin and metabolic syndrome. *Arter. Thromb. Vasc. Biol.* **24**, 29–33 (2004).
51. Patten, D. A. et al. OPA1-dependent cristae modulation is essential for cellular adaptation to metabolic demand. *EMBO J.* **33**, 2676–2691 (2014).
52. Morris, S. M. Jr. et al. Regulation of mRNA levels for five urea cycle enzymes in rat liver by diet, cyclic AMP, and glucocorticoids. *Arch. Biochem. Biophys.* **256**, 343–353 (1987).
53. Takiguchi, M. & Mori, M. Transcriptional regulation of genes for ornithine cycle enzymes. *Biochem. J.* **312**, 649–659 (1995).
54. Herkenne, S. et al. Developmental and tumor angiogenesis requires the mitochondria-shaping protein Opa1. *Cell Metab.* **31**, 987–1003.e1008 (2020).
55. Xie, F. et al. Identification of a potent inhibitor of CREB-mediated gene transcription with efficacious in vivo anticancer activity. *J. Med. Chem.* **58**, 5075–5087 (2015).
56. Heinonen, S. et al. Impaired mitochondrial biogenesis in adipose tissue in acquired obesity. *Diabetes* **64**, 3135–3145 (2015).

57. Pietilainen, K. H. et al. DNA methylation and gene expression patterns in adipose tissue differ significantly within young adult monozygotic BMI-discordant twin pairs. *Int. J. Obes.* **40**, 654–661 (2016).
58. Arriarán, S., Agnelli, S., Remesar, X., Fernández-López, J.-A. & Alemany, M. The urea cycle of rat white adipose tissue. *RSC Adv.* **5**, 93403–93414 (2015).
59. Ramirez, A. K. et al. Integrating extracellular flux measurements and genome-scale modeling reveals differences between brown and white adipocytes. *Cell Rep.* **21**, 3040–3048 (2017).
60. Matone, A. et al. Network analysis of metabolite GWAS hits: implication of CPS1 and the urea cycle in weight maintenance. *PLoS ONE* **11**, e0150495 (2016).
61. McKnight, J. R. et al. Beneficial effects of L-arginine on reducing obesity: potential mechanisms and important implications for human health. *Amino Acids* **39**, 349–357 (2010).
62. Fiedler, S. E. et al. Dimethyl fumarate activates the prostaglandin EP2 receptor and stimulates cAMP signaling in human peripheral blood mononuclear cells. *Biochem. Biophys. Res. Commun.* **475**, 19–24 (2016).
63. Naukkarinen, J. et al. Characterising metabolically healthy obesity in weight-discordant monozygotic twins. *Diabetologia* **57**, 167–176 (2014).
64. Pernas, L., Bean, C., Boothroyd, J. C. & Scorrano, L. Mitochondria restrict growth of the intracellular parasite *Toxoplasma gondii* by limiting its uptake of fatty acids. *Cell Metab.* **27**, 886–897 (2018).
65. Ritchie, M. E. et al. Limma powers differential expression analyses for RNA-sequencing and microarray studies. *Nucleic Acids Res.* **43**, e47–e47 (2015).
66. Bates, D., Mächler, M., Bolker, B. & Walker, S. Fitting linear mixed-effects models using lme4. *J. Stat. Softw.* https://doi.org/10.18637/jss.v067.i01 (2015).

Acknowledgements

We thank F. Caicci and F. Boldrin (EM Facility, Department of Biology, University of Padova) for electron microscopy samples preparation; F. Fuks (ULB, Brussels) for the gift of retroviral shKdm3a and shScramble expression vectors; Y. Capetanaki (Biomedical Research Foundation, Academy of Athens) for the gift of Platinum-E Retroviral Packaging Cell Line; S. Ciciliot (VIMM, Padova) for help with metabolic cages; M. Ghidotti (Department of Biology, University of Padova) for help with animal handling; R. Fabris, L. Busetto, M. Foletto, R. Serra, L. Prevedello, R. Bardini, C. Dal Prà, A. Belligoli, M. Sanna and C. Compagnin (University of Padova) for patient recruitment and adipose tissue biopsies collection; M. Rossato (University of Padova) for FLIR thermometry; and K. Lefkimmiatis and G. Di Benedetto (VIMM) for helpful discussions. The energy expenditure ANCOVA analysis was provided by the NIDDK Mouse Metabolic Phenotyping Centers (MMPC, www.mmpc.org) using their energy expenditure analysis page (http://www.mmpc.org/shared/regression.aspx) supported by grant nos DK076169 and DK115255. This work was supported by EFSD/Novo Nordisk Programme for Diabetes Research in Europe 2016 grant (L.S.), by Fondation Leducq TNE15004 (L.S.) and by Ministero dell'Istruzione, dell'Università e della Ricerca FIRB RBAP11Z3YA_005 and PRIN 2017BF3PXZ grants (L.S.); by PRIN 2010329EKE_005 (R.V.) and NanoBAT H2020-EU.1.3.3 MSCA-RISE-2015 (R.V.); and by Ministry of Education, University and Research (MIUR) Progetto Eccellenza (2018-2022) to the Department of Pharmacological and Biomolecular Sciences, University of Milan (N.M.). Twin research was supported by the Academy of Finland (grant nos 335443, 314383 and 272376) (K.P.); Finnish Medical Foundation (K.P.); Gyllenberg Foundation (K.P.); Novo Nordisk Foundation (grant nos NNF20OC0060547, NNF17OC0027232 and NNF10OC1013354) (K.P.) and Finnish Diabetes Research Foundation (K.P.).

Author contributions

C.B. and L.S. conceptualized the project, acquired funds and wrote the manuscript. C.B. performed and analysed most of the experiments and prepared figures. T.V. conceived and performed initial in vivo studies. F.F., F.S. and G.M. contributed to human and mouse studies. M. Medaglia performed qRT–PCR experiments. M. Gerdol and A.P. contributed to RNA-seq data analyses. L.P. advised on metabolic studies. M.A. and N.M. performed and analysed metabolomic experiments. M. Giacomello performed and analysed calcium imaging experiments. S. Herkenne provided reagents. K.H.P. and S. Heinonen examined twins and provided expression and clinical data. M. Muniandy, M.O. and E.C. analysed twins expression data. R.V. provided bariatric surgery studies. L.S. supervised the project. All authors edited the manuscript.

Competing interests

The authors declare no competing interests.

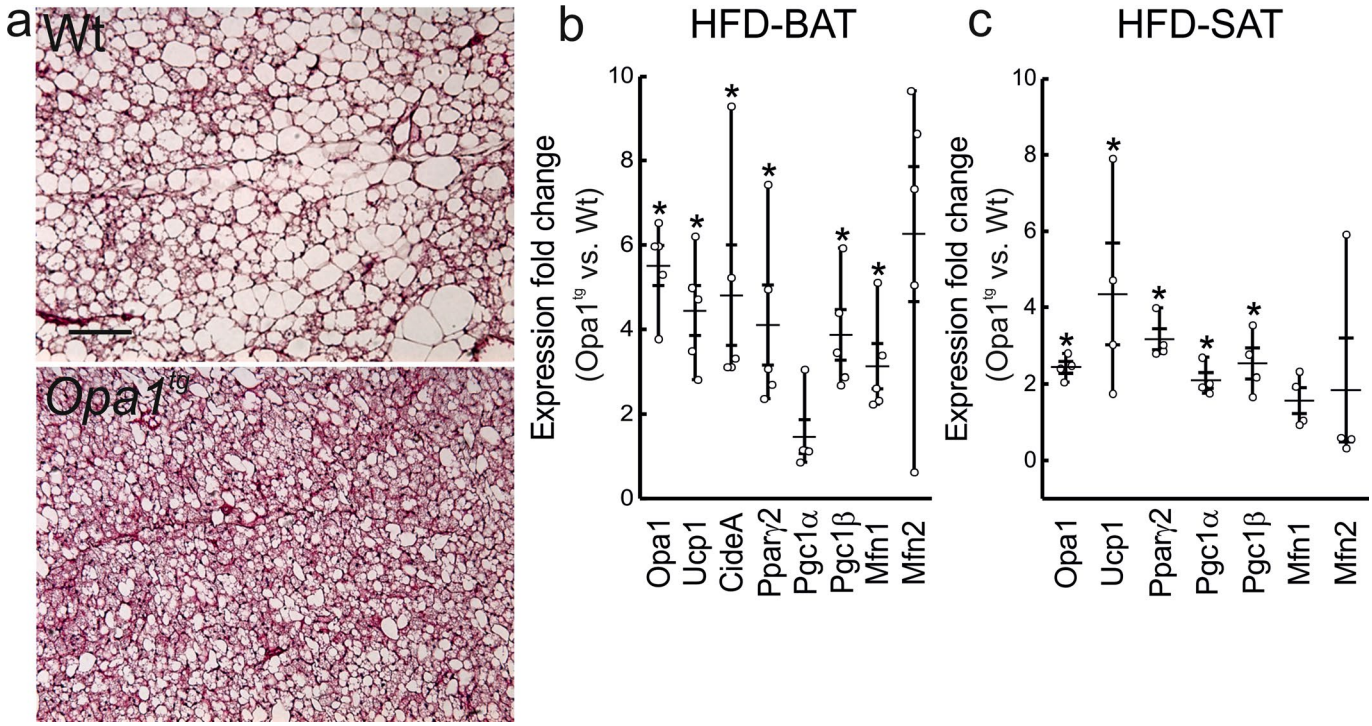

Extended Data Fig. 1 | Opa1 increases thermogenic activity. (**a**) Representative Haematoxylin-Eosin stained sections of BAT from HFD-fed Wt and *Opa1*^{tg} mice (n = 8/genotype). Scale bar: 200 µm. (**b**,**c**) Expression fold change (*Opa1*^{tg} vs. Wt) of thermogenic, adipogenic and mitochondrial gene markers in BAT (b) SAT (c) of HFD-fed *Opa1*^{tg} (n = 5) and Wt mice (n = 4). Dots represent individual mice, I-shaped boxes mean ± SEM; whiskers indicate the 10th-90th percentile. Two-tailed Mann-Whitney U test in HFD-BAT: p = 0.037 for Opa1, Ucp1, Mfn1, p = 0.019 for CideA, Pparγ2 Pgc1β. Two-tailed Mann-Whitney U test in HFD-SAT: p = 0.03 for Opa1, Ucp1, Pparg2, Pgc1α, Pgc1β.

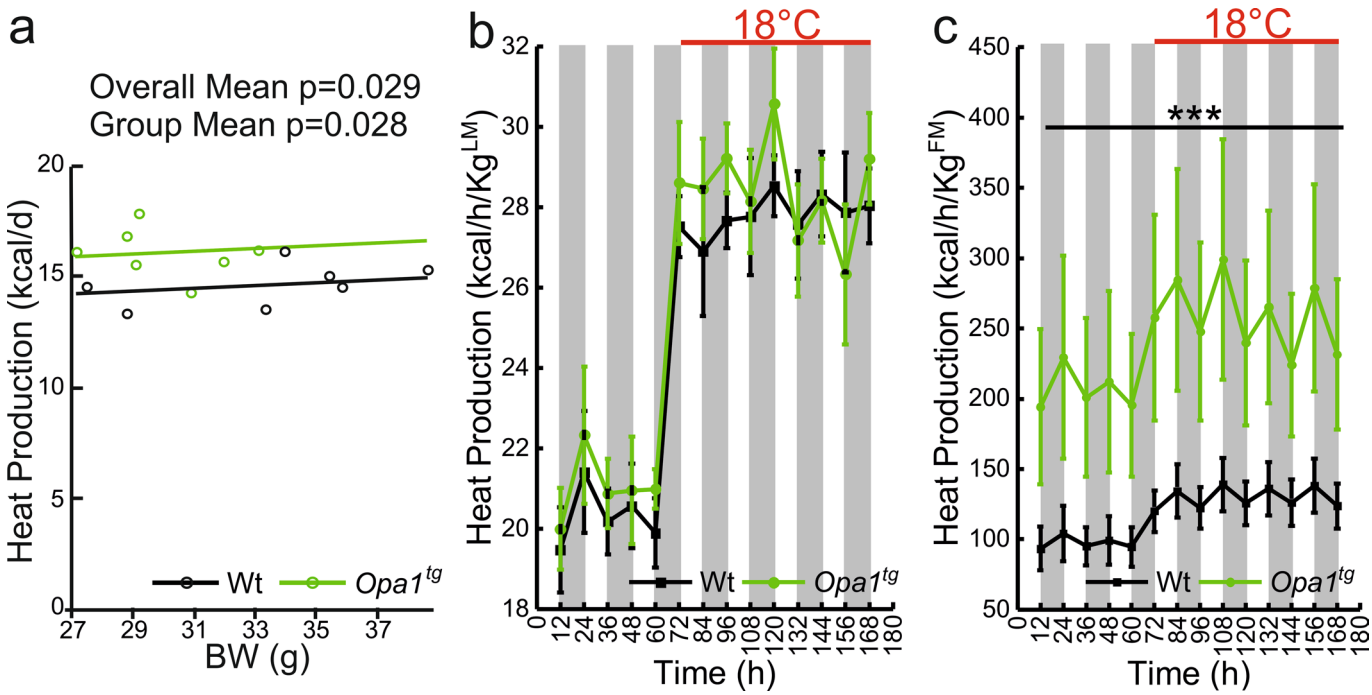

Extended Data Fig. 2 | Heat production and ANCOVA analysis of heat production in Opa1^{tg} mice. (**a**) Plot of ANCOVA predicted mean energy expenditure for total body weight (BW) values in *Opa1^{tg}* and Wt mice. Data are from experiments in Fig. 3h (n = 7 mice/genotype). Multiple linear regression analysis of the impact of body mass covariate on energy expenditure was calculated using the MMPC Web Tool at the MMPC Energy Expenditure Analysis Page. Overall p value refers to significance of the ANCOVA-adjusted comparison when BW was taken over both *Opa1^{tg}* and Wt groups. Group p-value refers to significance of the ANCOVA-adjusted comparison when BW was taken over the two individual *Opa1^{tg}* and Wt groups. (**b, c**) Average±SEM of heat release normalized by lean mass (LM, b) or fat mass (FM, c) in light and dark (indicated as gray vertical stripes on the graph) cycles recorded in male mice of the indicated genotypes at 24 °C and at the indicated temperature. n = 7 mice/genotype. ***, p = 4.1×10^{-4} (basal heat production at 24 °C) and 9.7×10-5 (at 18 °C) in one-way repeated measures ANOVA.

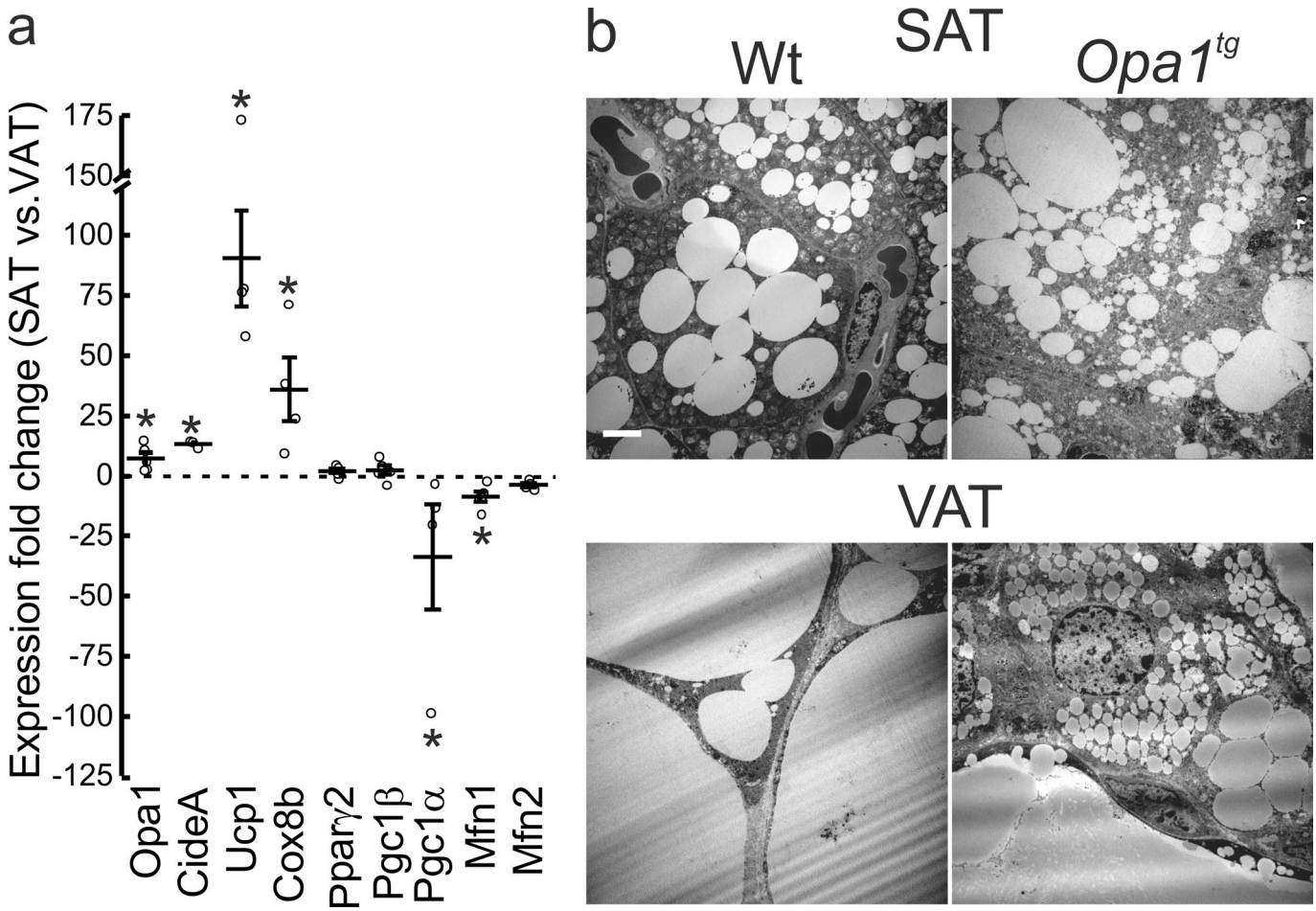

Extended Data Fig. 3 | Opa1 promotes browning of white adipocytes. (**a**) Expression fold change (SAT vs. VAT) of the indicated BAT specific and mitochondrial genes in Wt mice (n = 4-5). Dots indicate individual mice, center lines mean, whiskers SEM. *, p = 0.019 for Opa1, Ucp1, Pgc1α; p = 0.03 for Cox8b; p = 0.05 for CideA. (**b**) Electron microscopy (EM) images from SAT and VAT of Wt and *Opa1^{tg}* mice treated for 5 days with 10 mg/kg CL316,243 (CL), administered i.p. every day (n = 6 independent experiments). Scale bar: 5 μm.

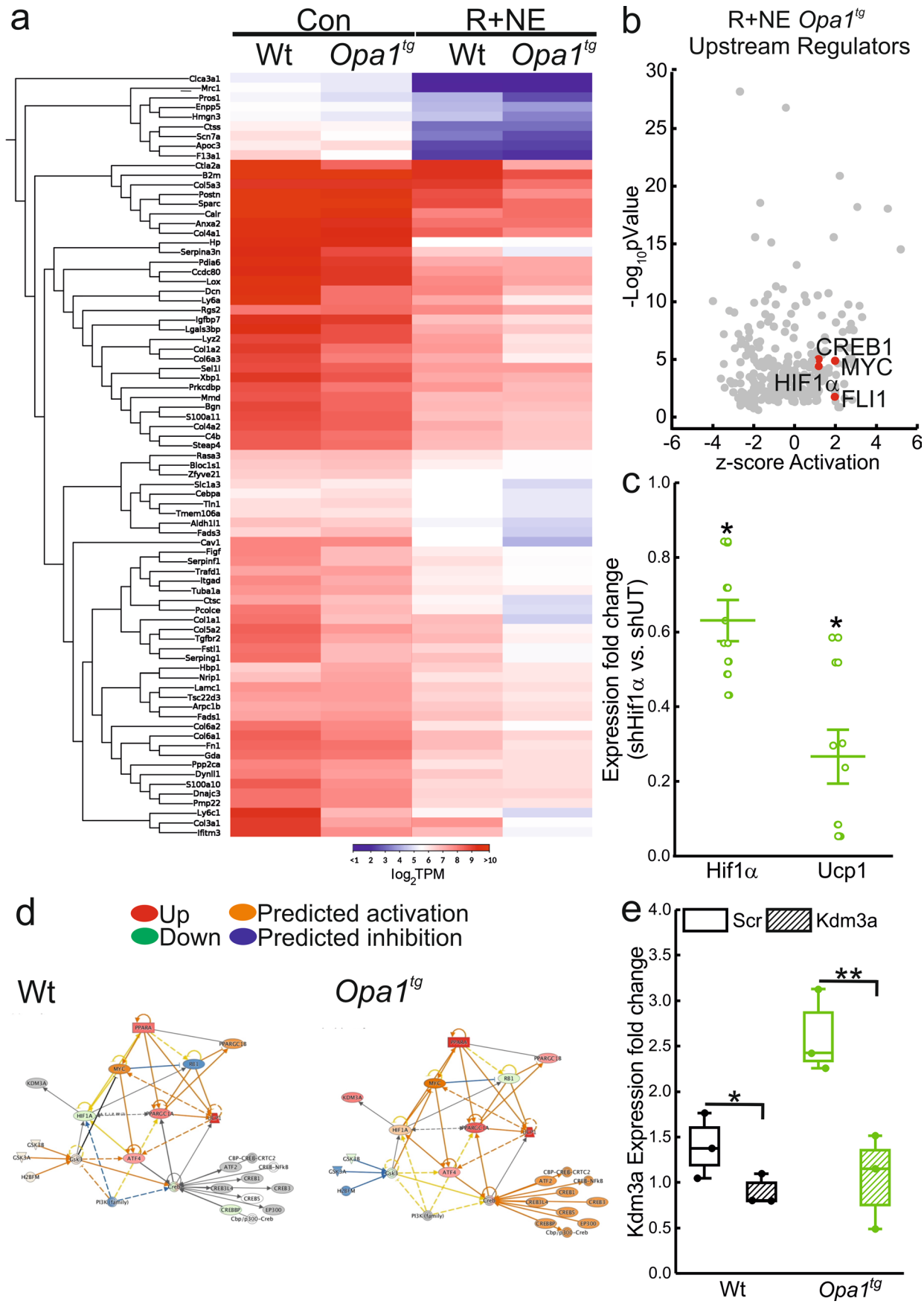

Extended Data Fig. 4 | See next page for caption.

Extended Data Fig. 4 | Analysis of master gene regulators in differentiating Opa1^{tg} preadipocytes. (**a**) Heat map of the expression levels of the *Opa1*-specific downregulated genes subset identified in Fig.4h. Each column corresponds to the indicated sample. The dendrogram clustering on the Y-axis groups genes with similar expression profiles. Gene expression levels are indicated per each row. (**b**) Upstream regulators for the DEGs dataset in Fig.4h by Upstream Regulator Analysis in IPA. y-axis corresponds to the Log_{10} (p-Value), and the x-axis displays the z-score activation values. (**c**) Expression fold change of the indicated genes in Opa1^{tg} pre-adipocytes transduced with shRNAs against *Hif1α* (shHif1α) or an untargeted control sequence (shUT) and differentiated into brite adipocytes (n = 10 independent experiments). Dots indicate individual experiments, center lines the mean, whiskers SEM. *, p = 0.001 for Hif1α and 0.003 for Ucp1 in a two-tailed Mann-Whitney U test. (**d**) Selected DEGs identified in Fig. 4i were used to identify functional relationships among selected genes by IPA. (**e**) Kdm3a expression fold change (brite vs. preadipocytes). Pre-adipocytes of the indicated genotype transduced with the indicated shRNA were differentiated into brite adipocytes. N = 3 independent experiments from 6 pooled *Opa1^{tg}* or Wt mice/experiment. Dots indicate individual experiments, box represents mean ± SEM, whiskers the 10th-90th percentile.; *p = 0.04, **p = 0.01 in two-tailed sample t-test.

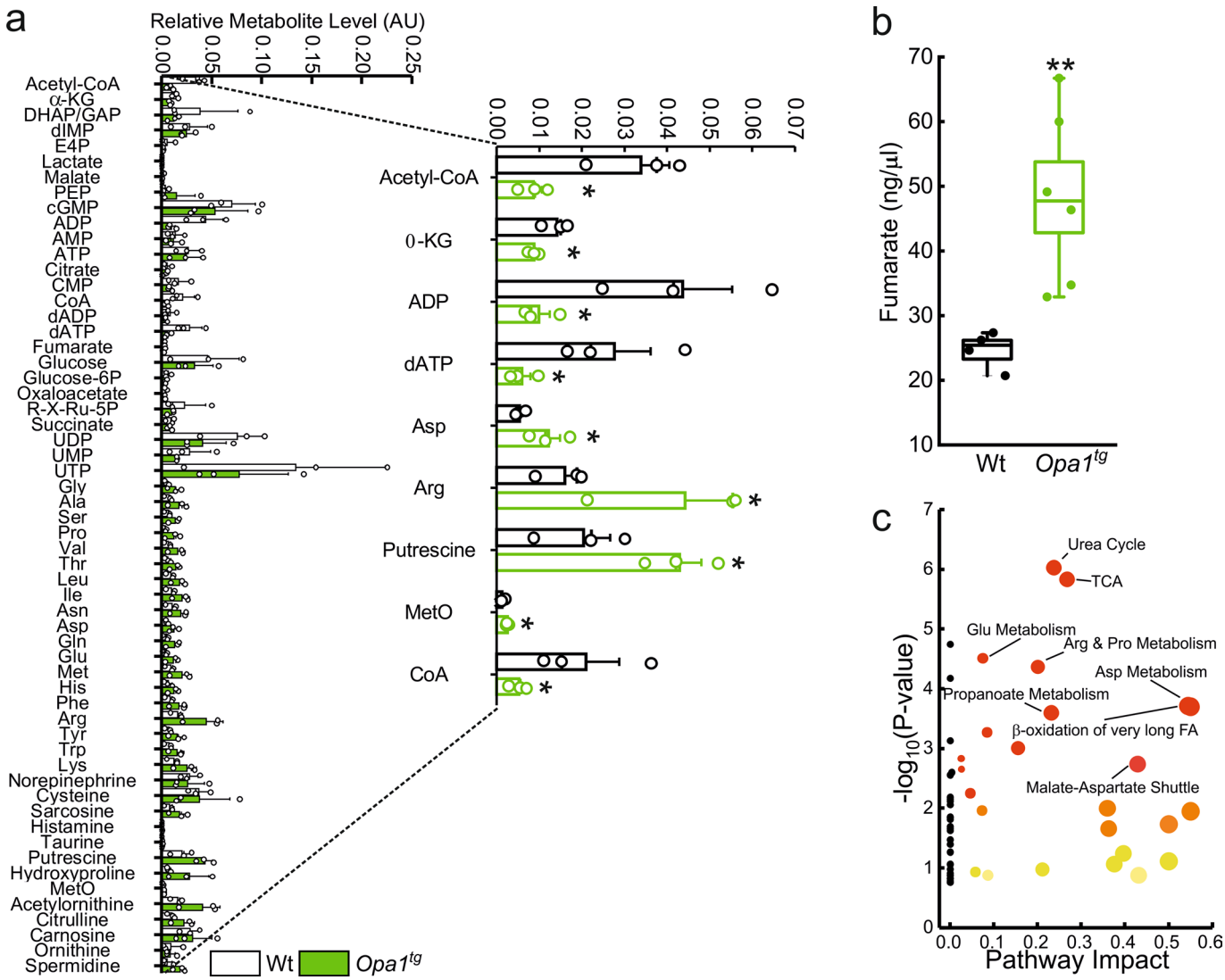

Extended Data Fig. 5 | Opa1 controls fumarate levels *in vivo*. (**a**) Average+SEM of metabolite levels in mature adipocytes from SAT of Wt and *Opa1*^{tg} mice (n = 3). Metabolites with a significantly different mean concentration in *Opa1*^{tg} vs Wt adipocytes are highlighted in the inset. * p = 0.049 in a Kruskal-Wallis ANOVA test. (**b**) Fumarate levels in 40 mg of SAT isolated from Wt (n = 4) and *Opa1*^{tg} (n = 6) mice. Box represents mean ± SEM, whiskers the 10th-90th percentile. **p = 0.014 in a two-tailed Mann-Whitney U test. (**c**) Metabolites in (**a**) and (**b**) were analyzed using the Pathway Analysis module of MetaboAnalyst tool. Red dots show the top significantly relevant pathways.

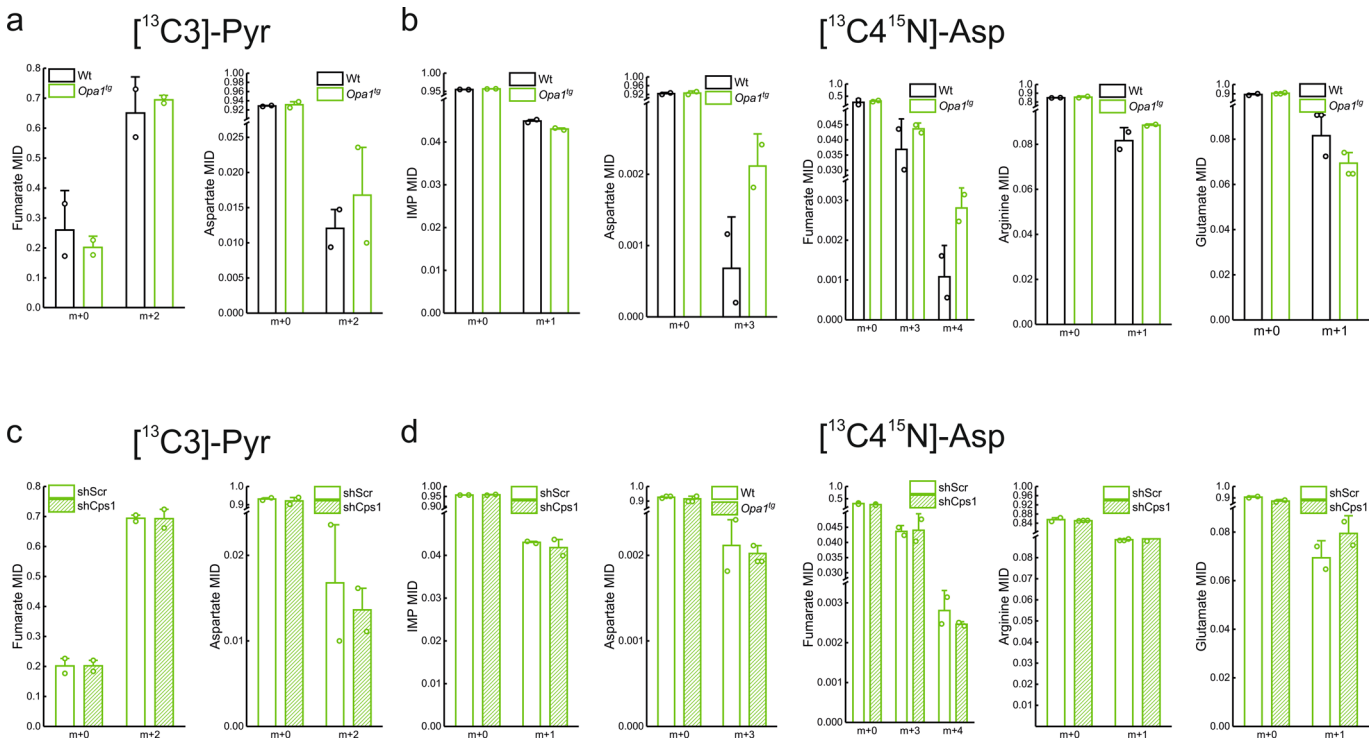

Extended Data Fig. 6 | Mass isotopomer distribution in flux analysis experiments. (**a**) Mass isotopomer distribution (MID) of fumarate and aspartate in *Opa1*^{tg} and Wt preadipocytes following [^{13}C3]-pyruvate infusion. (**b**) Mass isotopomer distribution of IMP, Aspartate, Fumarate, Arginine, Glutamate in *Opa1*^{tg} and Wt preadipocytes following [^{13}C4,^{15}N]-L-aspartic acid infusion. (**c**) Mass isotopomer distribution of fumarate and aspartate in *Opa1*^{tg} preadipocytes transduced with control (shScr) shRNA and against Cps1 (shCps1) following [^{13}C3]-pyruvate infusion. (**d**) Mass isotopomer distribution of IMP, Aspartate, Fumarate, Arginine, Glutamate in *Opa1*^{tg} preadipocytes transduced with control (shScr) shRNA and against Cps1 (shCps1) following [^{13}C4,^{15}N]-L-aspartic acid infusion. In all graphs, unlabeled (m + 0) and labeled isotopomers are shown. Bars represents the average value from 2 indicated (dots) independent measurements (n = 4 pooled mice/genotype/experiment).

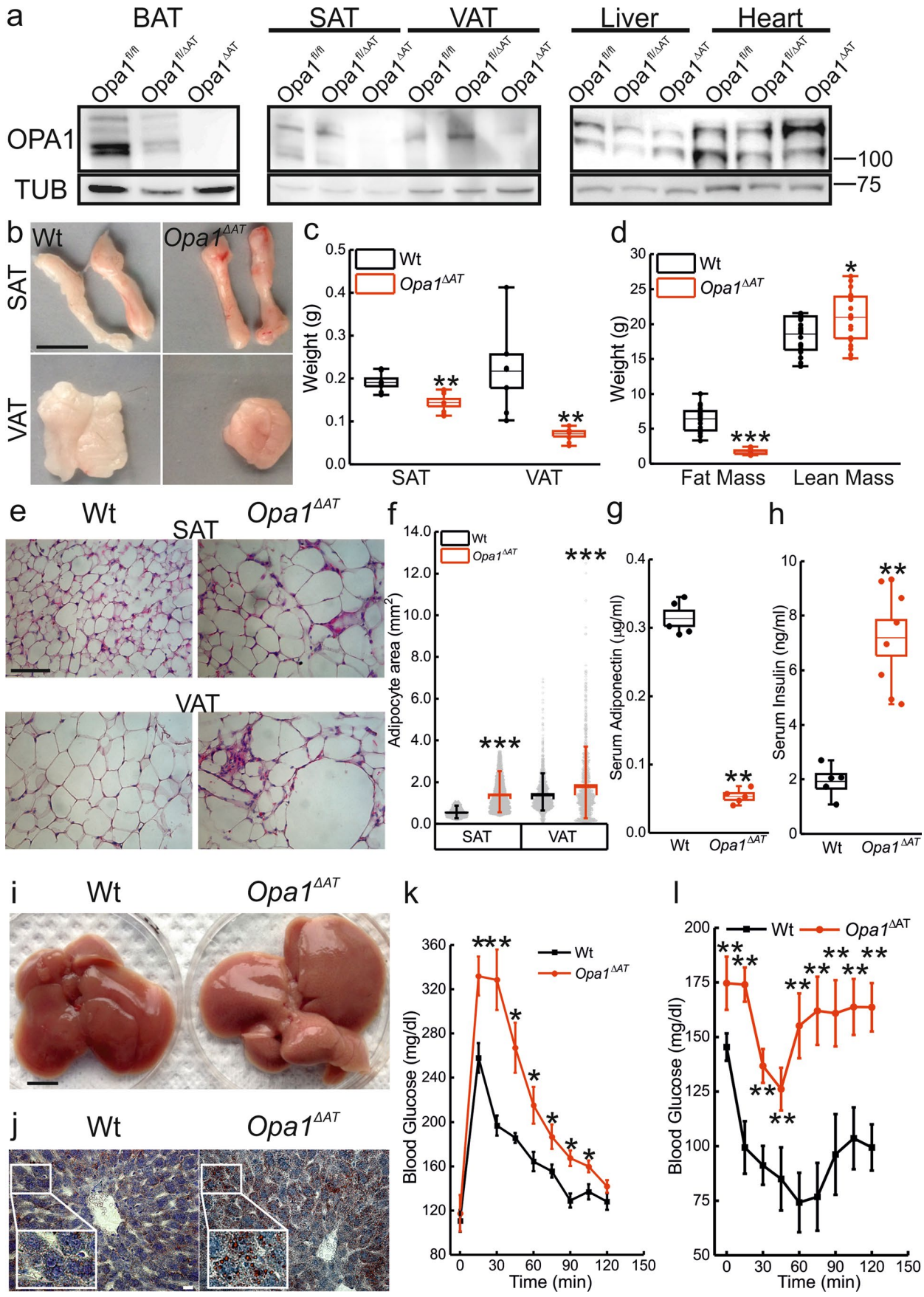

Extended Data Fig. 7 | See next page for caption.

Extended Data Fig. 7 | Adipocyte *Opa1* deletion causes lipoatrophy and metabolic dysfunction. (**a**) Equal amounts of protein (20 μg) from brown adipose tissue (BAT), subcutaneous (SAT) and visceral (VAT) white adipose tissues, heart and liver lysates from mice of the indicated genotypes were separated by SDS-PAGE and immunoblotted using the indicated antibodies (n = 7/genotype). (**b**) Representative photographs of SAT and VAT from control and *Opa1*$^{\Delta AT}$ mice (n = 7/genotype). Scale bar: 1 cm. (**c**) Box-dot plots of SAT and VAT weights from control and *Opa1*$^{\Delta AT}$ mice (n = 7-8). **, p = 0.009 *Opa1*$^{\Delta AT}$ vs. Wt SAT; p = 0.001 *Opa1*$^{\Delta AT}$ vs. Wt VAT in a two-tailed Mann-Whitney U test. (**d**) Body composition assessed by EchoMRI in Wt (n = 23) and *Opa1*$^{\Delta AT}$ (n = 20) mice. *, p = 0.04 *Opa1*$^{\Delta AT}$ vs. Wt lean mass; ***, $p = 2.2\times10^{-8}$ *Opa1*$^{\Delta AT}$ vs. Wt fat mass in a two-tailed Mann-Whitney U test. (**e**) Representative Hematoxylin-Eosin staining of SAT and VAT from control and *Opa1*$^{\Delta AT}$ mice (n = 7/genotype). (**f**) Box-dot plots of adipocytes area in control and *Opa1*$^{\Delta AT}$ mice. (n > 1000 adipocyte/mouse; 4 mice/genotype). ***, $p = 1\times10^{-5}$ in a two-tailed Mann-Whitney U test between groups. (**g**,**h**) Box-dot plots of Serum Adiponectin (g) and Insulin (h) levels measured by ELISA in control and *Opa1*$^{\Delta AT}$ mice (n = 5-8). **, p = 0.01 for Adiponectin and p = 0.004 for Insulin in a two-tailed Mann-Whitney U test. (i) Representative photographs of livers from control and *Opa1*$^{\Delta AT}$ mice (n = 7/genotype). Scale bar: 1 cm. (j) Representative Oil Red O staining of livers from control and *Opa1*$^{\Delta AT}$ mice (n = 7/genotype). Red indicates lipid deposits. Inset is magnified 2X. Bar: 20 μm. (k) Average±SEM of blood glucose levels following an i.p. glucose tolerance test (GTT) performed on control and *Opa1*$^{\Delta AT}$ mice (n = 5-6). **, p < 0.01; *, p < 0.05 in a two-tailed Mann-Whitney U test. (l) Average±SEM of blood glucose levels following an i.p. insulin tolerance test (ITT) performed on control and *Opa1*$^{\Delta AT}$ mice. **, p < 0.01 in a two-tailed Mann-Whitney U test. In panels c, d, g, h dots represent the individual measurements, boxes mean ± SEM, whiskers the 10th-90th percentile.

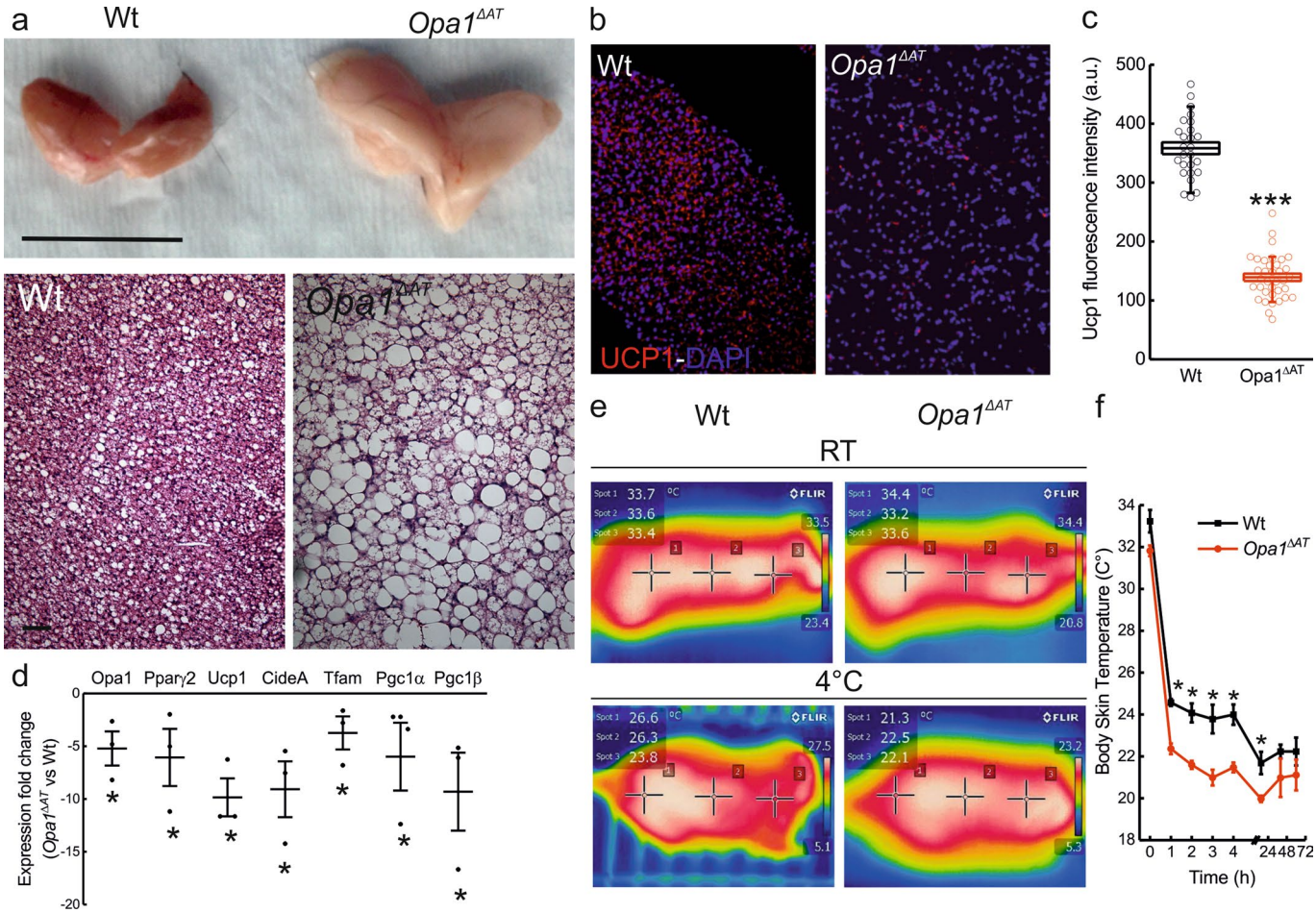

Extended Data Fig. 8 | Adipocyte *Opa1* deletion impairs BAT thermogenic activity. (a) Top: Gross morphology of representative BAT from Wt and *Opa1*$^{\Delta AT}$mice. Scale bar: 1 cm. Bottom: representative Hematoxylin-Eosin staining of BAT mice of the indicated genotype. Scale bar: 50 µm. (b) Representative fluorescence images of Wt and *Opa1*$^{\Delta AT}$ BAT sections immunostained for UCP1 (red) and with DAPI (blue) (n = 3/genotype). Scale bar: 50 µm. (c) Box-dot plots of UCP1 staining intensity in BAT sections of Wt and *Opa1*$^{\Delta AT}$ mice (n = 27 sections over 3 mice/genotype). Dots represent individual sections, boxes SEM, center line mean, whiskers the 10th-90th percentile. ***, p = 2.6×10^{-11} in a two-tailed Mann-Whitney U test. (d) Fold change (*Opa1*$^{\Delta AT}$ vs. Wt) of the indicated genes in Wt and *Opa1*$^{\Delta AT}$ BAT (n = 3 mice/genotype). Centre line: mean; whiskers: SEM. *, p = 0.049 for Opa1, Pparγ2, CideA, Tfam, Pgc1α and p = 0.043 for Ucp1 in a Kruskal-Wallis ANOVA test. (e) Representative pseudocolored dorsal view images of IR thermography of conscious male Wt and *Opa1*$^{\Delta AT}$mice. Images were collected at room temperature (RT, 22–23 °C) and 1 h after cold exposure (4 °C). (f) Average±SEM of body skin temperature measured at the indicated times in experiments as in (e) (n = 4 mice/genotype). *, p < 0.05 in a two-tailed Mann-Whitney U test.

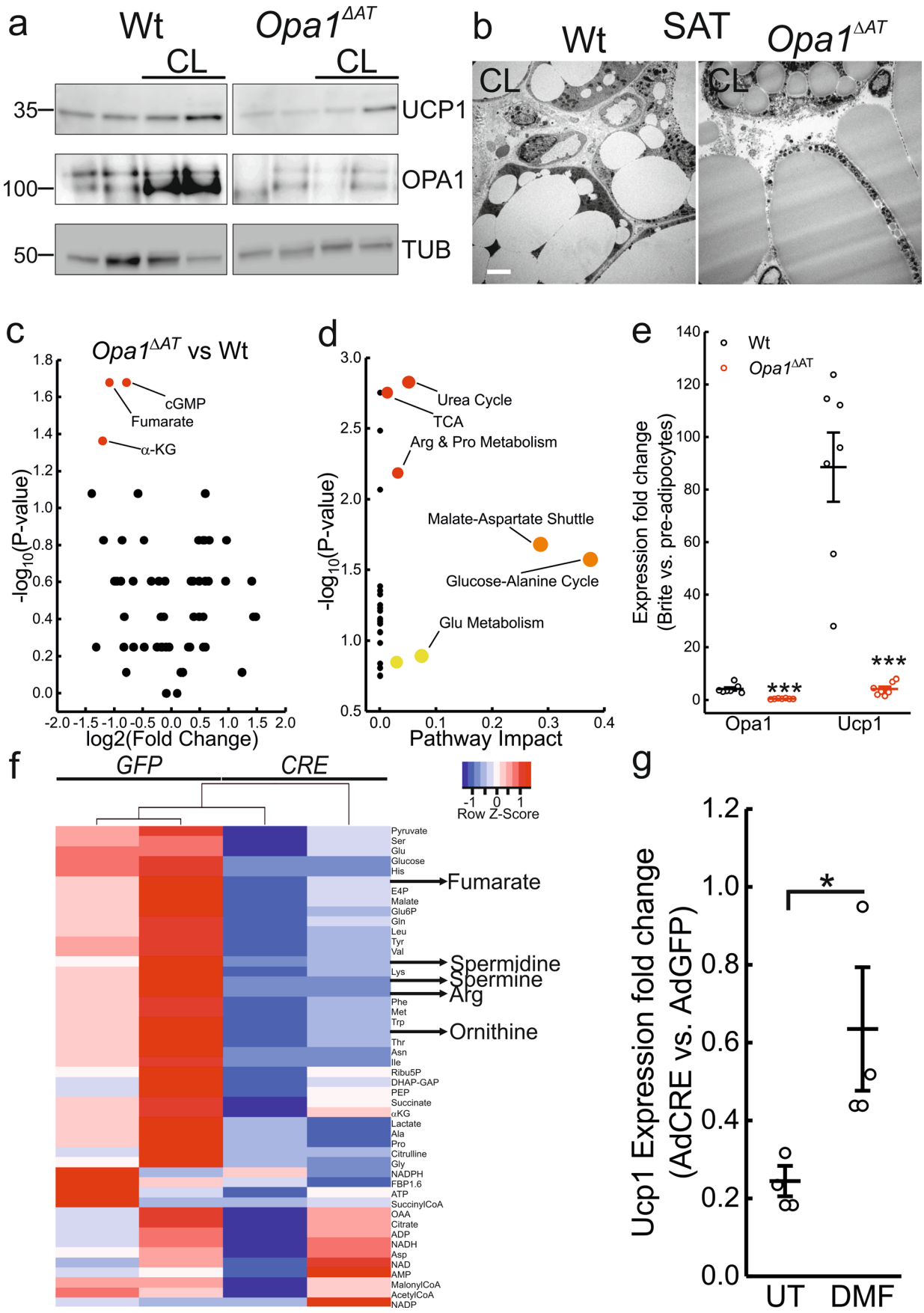

Extended Data Fig. 9 | See next page for caption.

Extended Data Fig. 9 | Adipocyte *Opa1* deletion impairs preadipocytes browning by reduction in fumarate levels. (a) Equal amounts of protein (20 µg) from SAT isolated from littermates of the indicated genotype treated where indicated with the beta-3 adrenergic agonist CL-316,243 (CL; 10 mg/kg) for 5 days were separated by SDS-PAGE and immunoblotted using the indicated antibodies. TUB: tubulin. Each lane corresponds to an individual mouse. (b) Electron microscopy (EM) images from SAT of control and *Opa1*$^{\Delta AT}$ mice treated for 5 days with ip injection of 10 mg/kg of CL316,243 (CL) every day. Scale bar: 5 µm. (c) Volcano plot of a metabolomic analysis of SAT from Wt and *Opa1*$^{\Delta AT}$ mice (n = 4). The red dots indicate significantly different metabolites. (d) Metabolites in (c) were analyzed using the Pathway Analysis module of MetaboAnalyst tool. Red dots show the top significantly relevant pathways. (e) Box-dot plots of *Opa1* and *Ucp1* expression fold change (brite vs. preadipocytes) in Wt and *Opa1*$^{\Delta AT}$ SAT pre-adipocytes differentiated into brite adipocytes. Data are normalized for β-actin gene expression, calculated by ΔΔCT (n = 7). ***, $p = 7.9\times10^{-4}$ for Opa1 and $p = 4.1\times10^{-4}$ for Ucp1 in a two-tailed Mann-Whitney U test. (f) Heat map of hierarchical clustering by Pearson Correlation of metabolomics analysis of brite-differentiated white preadipocytes infected with AdCre or AdGFP as control. Each column represents one independent experiment. (g) Dot plots of Ucp1 relative expression in pre-adipocytes isolated from *Opa1*$^{fl x fl x}$ mice and differentiated into brite adipocytes after adenovirus-mediated infection with Cre-GFP or GFP as control. Data are expression fold change normalized for β-actin gene expression, calculated by ΔΔCT (n = 3). *, $p < 0.05$ Kruskal-Wallis ANOVA test ($p = 0.049$). In e,g dots represent biologically independent experiments, I-shaped boxes mean ± SEM, whiskers the 10th-90th percentile.

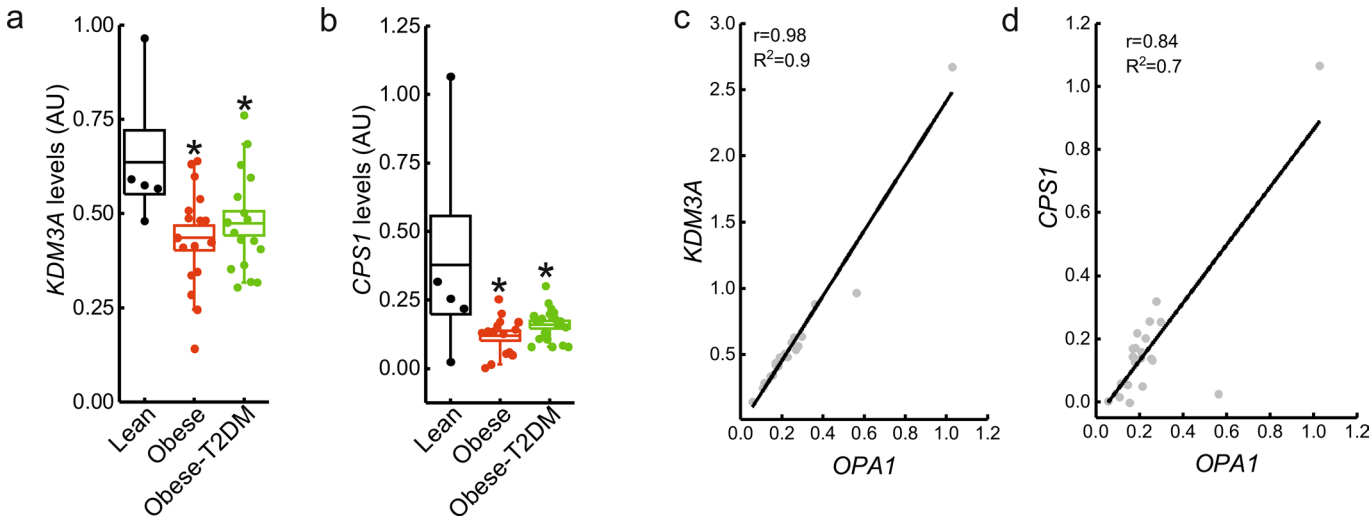

Extended Data Fig. 10 | KDM3a and CPS1 are reduced in WAT of obese individuals. (a,b) Box-dot plots of quantitative PCR analysis of *KDM3A* (a) and *CPS1* (b) transcripts from abdominal wall fat pad biopsies of 5 lean subjects, 15-17 obese normoglycemic subjects (Obese), and 17-19 obese diabetic patients (Obese-T2DM). Data are normalized for the expression of S18. *, p = 0.01 (Obese vs. Lean) and p = 0.03 (Obese-T2DM vs. Lean) for *KDM3A* and p = 0.02 for *CPS1* in a one way ANAOVA test. (c,d) Pearson correlation analysis of *OPA1* with *KDM3A* (c) and *CPS1* expression (d) in lean and individuals with obesity as in (a,b).